Energy Conversion and Management 283 (2023) 116941

Contents lists available at ScienceDirect

Energy Conversion and Management

journal homepage: www.elsevier.com/locate/enconman

Thermo-economic analysis of a novel partial cascade organic-steam Rankine cycle

Pengcheng Li [a,c], Tongle Qian [a], Jing Li [b,*], Haiwei Lin [a], Yandong Wang [d], Gang Pei [e], Desuan Jie [a], Dongming Liu [a]

[a] School of Automotive and Transportation Engineering, Hefei University of Technology, 193 Tunxi Road, Hefei, China
[b] Center for Sustainable Energy Technologies, Energy and Environment Institute, University of Hull, Hull HU6 7RX, UK
[c] DONGFANG ELECTRIC Dongfang Boiler Group CO., LTD., 150 Huangjue Ping, Wuxing Street, Zigong, China
[d] Hefei General Machinery Research Institute, 888 Changjiang Road ,Hefei, China
[e] Department of Thermal Science and Energy Engineering, University of Science and Technology of China, 96 Jinzhai Road, Hefei, China

ARTICLE INFO

Keywords:
Solar power tower system
Organic Rankine cycle
Steam Rankine cycle
Molten salts
Biphenyl/diphenyl oxide mixture
Equivalent payback period

ABSTRACT

Conventional heat batteries and concentrated solar power systems adopt subcritical steam Rankine cycles (SRCs) to avoid the technical challenges of supercritical cycles. The water evaporation temperature of 310–337 °C and live steam pressure of 10–14 MPa limit the cycle efficiency (around 42%). This paper proposes a novel partial cascade organic-steam Rankine cycle (ORC-SRC) system to increase the fluid evaporation temperature and thermal efficiency. The ORC-SRC uses a mixture of biphenyl and diphenyl oxide as the top cycle fluid. The mixture absorbs heat from the molten salts and evaporates at about 400 °C to drive a turbine, and then the exhaust vapor releases heat to the bottom SRC. The ORC contributes to saturated steam generation, and molten salts supply the rest heat to the SRC through the steam superheater and reheater. The fundamentals of the system are illustrated, and mathematical models are built. Thermo-economic performance of the system is investigated. The results show that the proposed system significantly increases the average temperature of the power fluid in the heating process, leading to a maximum cycle efficiency of 45.3%. Meanwhile, the moderate live steam pressure of 7.44 MPa in the SRC reduces the leakage loss of the high-pressure turbine and equipment costs. Despite a smaller temperature drop of molten salts during discharge, the equivalent payback period of the ORC-SRC is within 4 years.

1. Introduction

Concentrated solar power (CSP) generation is an effective way to cope with the energy crisis due to its bulk and clean electricity generation capability. The main advantages of the CSP technology against other renewable technologies, such as photovoltaic or wind power generation, are large-scale and economical heat storage and the potential for hybridization. These enable CSP systems to work with higher capacity factors and dispatchability [1]. The installed CSP capacity reached 6,128 MWe worldwide in 2020 [2]. The current most mature technology employs parabolic trough collectors (PTCs) and solar power towers (SPTs) to harvest energy. They represent 97% of the installed capacity [3,4]. Although the SPT has a higher capacity cost and stricter technical requirements, it accounts for 61.51% of the plants under construction or development due to its relatively high efficiency [4], low levelized cost of electricity (10.9 ¢/kWhe) [3,5], and large capacity factor (55 for a 10 h storage case) [6]. The SPT is expected to lead the market and will be the most developed CSP option in the near future [7,8].

SPTs, also known as central receiver systems, are set up by a heliostat field that reflects solar radiation into a central receiver located atop a tower, where a fluid (commonly molten salts or steam) carries away the heat and then drives a steam Rankine cycle (SRC) to produce electricity. The heliostats track the sun with two axes, and the most advanced receivers can reach 1000 °C [9]. Since the first commercial plant (11 MWe Planta Solar 10) started operation in 2007, the SPT systems have shown explosive growth. The representative projects include the 377 MWe Ivanpah Solar Electric Generating System, which is the largest operational one consisting of three subtowers [6,10], and the 110 MWe Crescent Dunes ranking the second largest SPT incorporating a 10-hour molten salts storage [10,11], and the 100 MWe Shouhang Dunhuang II

* Corresponding author.
E-mail address: Jing.Li@hull.ac.uk (J. Li).

https://doi.org/10.1016/j.enconman.2023.116941
Received 6 December 2022; Received in revised form 6 February 2023; Accepted 14 March 2023
Available online 22 March 2023

Nomenclature

A	heat exchanger area, m^2
B	coefficient
C	cost, $/ coefficient
c_p	specific heat, J/kg·K
Ex	exergy, kW
F_M	correction factor
F_P	pressure factor
h	enthalpy, kJ/kg
I	exergy loss, kW
K	coefficient
M	mass, tonne
m	mass flow rate, kg/s
p	pressure, MPa
P	pump
P	price, $
q	heat transfer, kW
Q	heat obtained by PTC, kJ
S	entropy generation, kW/K
s	specific entropy, kJ/(kg·K)
T	temperature, K
t	temperature, °C
v	specific volume, m^3/kg
W	work, kWh
Y	excess annual electricity yield, kWh
y	steam wetness, %
w	work, kW
ε	device efficiency, %
η	efficiency, %
η_{ex}	exergy efficiency, %
ρ	density, kg/m^3
λ	thermal conductivity, J/kg·℃
μ	dynamic viscosity, mPa·s

Abbreviation

BDO	biphenyl/diphenyl oxide
CEPCI	Chemical Engineering Plant Cost Index
CF	closed feedwater
CSP	concentrated solar power
EPP	equivalent payback period
HP	high-pressure
HTT	high temperature tank
IHX	internal heat exchanger
LP	low-pressure
LTT	low temperature tank
ORC	organic Rankine cycle
ORC-SRC	organic-steam Rankine cycle
OF	open feedwater
PTC	parabolic trough collector
SPT	solar power tower
SRC	steam Rankine cycle

Subscript

I	system I
II	system II
0,1,2…	number
a	ambient
add	additional
ann	annual
av	average
b	basic
BM	the bare module
e	electricity
evap	evaporator
ex	exergy
EHST	equivalent hot side temperature
filed	heliostat field
gHT	generatorhigh-pressure turbine
LT	low-pressure turbine
min	minimum
ms	molten salts
OT	ORC turbine
opt	optimal
P	pump
pc	power cycle
pre	preheater
re	reheater
rec	receiver
ref	reference project
s	isentropic
sh	superheated
sl	saturated liquid
st	steam
sun	sun
sup	superheater
sv	saturated vapor

equipped with the highest tower and 11-hour storage, enabling 24 h of continuous power generation [11,12]. Details of some operational SPT stations are provided in Table 1.

Notably, all commercial SPT plants operate at subcritical conditions, and the vast majority employ molten salts as the heat transfer and dual-tank storage fluid [10,13]. State-of-the-art molten salts operate below 565 °C, and higher temperature operation will require new salt mixtures or other suitable heat carriers like particle silos [14]. Barriers like corrosive nature, large heat loss, low thermal conductivity, and poor reliability have yet to be tackled before using new heat transfer/storage media commercially. Supercritical SRCs can increase the average temperature of water/steam in the heating process and is potentially more efficient. However, they have not been applied in mainstream SPT plants due to unsolved technical problems, including:

First, the power capacity of a CSP plant is too small for a supercritical SRC. A low specific volume of steam accompanies a supercritical pressure (greater than 22 MPa). The leakage loss increases with a narrower steam blade path at the turbine inlet. For this reason, the typical supercritical steam turbines are more powerful above 400 MWe [15,16]. It is unachievable by a CSP plant as the size of the heliostat field and receiver (rated at approximately 160 MWe) restricts its capacity [17]. A more feasible option for capacity enhancement is to combine a supercritical SRC-SPT system with a coal-fired plant [18].

Second, supercritical cycles set up higher requirements for materials. High-pressure and intermediate-pressure turbines are generally made of special high-alloy steel (Cr, Mo, and V). The first stages of these turbines have an element of nickel to address the thermal loads resulting from the temperature drop during expansion [19]. The high operating pressure increases stringent requirements for the material selection, design, and operation of the turbomachinery, heat exchangers, and receiver [20]. As a result, the equipment cost rises, which may offset the benefit of high efficiency.

Third, supercritical power plants face the challenge of fast frequency response [21]. Energy storage is essential for flexible operation and rapid frequency responses in power generation, which can be achieved by using a drum to regulate the opening degree of the turbine expansion

Table 1
Details of some operational SPT stations [11].

SPT stations	Nominal capacity (MWe)	SRC evaporation pressure (MPa)	Location	Start year
Planta Solar 10 - PS10	11	4.5	Spain	2007
Planta Solar 20 - PS20	20	4.5	Spain	2009
ACME Solar Tower	2.5	6	India	2011
Lake Cargelligo	3	5	Australia	2011
Greenway CSP Mersin Tower Plant	1.4	5.5	Turkey	2012
SUPCON Delingha 10 MWe Tower	10	8.83	China	2013
Ivanpah Solar Electric Generating System	377	16	United States	2014
Crescent Dunes Solar Energy Project	110	11.5	United States	2015
Shouhang Dunhuang Phase II – 100 MWe Tower	100	12.6	China	2018
SUPCON Delingha 50 MWe Tower	50	13.2	China	2018
CEEC Hami – 50MWe Tower	50	14	China	2019

valves and make necessary primary responses. Unlike a subcritical cycle with drum-type units, the supercritical cycle does not have an energy storage drum in the boiler. Moreover, high steam pressure leads to thicker pipe walls and turbine casings, further prolonging startup time. The above problem is particularly challenging to solar thermal power generation as the plant will need to restart on many days throughout the year.

For the above considerations, state-of-the-art SPT plants use subcritical SRCs for power conversion. The design SRC efficiency usually ranges from 41.2% [3] to 41.98% [22], and the live steam temperature and pressure are usually 540 °C and 10–16 MPa [23]. The SRC efficiency is restricted by a relatively low water evaporation temperature of about 330 °C despite a high molten salt temperature of 560 °C. Water has large latent heat for evaporation. For instance, the latent heat is 1140 kJ/kg at 330 °C, which accounts for more than 50% of the total heat input to the SRC.

The subcritical SRCs are also preferable for power conversion in heat batteries. Batteries can support high levels of variable renewable electricity by storing surplus electricity at the time of strong radiation or wind and releasing it later, for instance, to meet the peak demand. They will play a crucial role in balancing the future electricity grid. Heat batteries are an emerging technology for inexpensive and site-independent electrical storage and have the potential to solve the global storage problem [24,25]. Similar to CSP plants, current heat batteries employ subcritical SRCs. For instance, Chile recently proposed replacing a coal-fired power station with a heat battery plant. The project would use renewable energy technology to heat salts and subcritical SRC to convert thermal energy into power [26].

In order to overcome the limitation in the water evaporation temperature and increase the SRC efficiency while avoiding the challenges of supercritical SRC, this paper proposes a partial cascade organic-steam Rankine cycle (ORC-SRC) for SPT and heat battery applications. It uses an organic Rankine cycle (ORC) as a top cycle for the SRC. The ORC technology has significantly matured, with a 46% increment in the installed plants over the past five years [27]. It has become state-of-the-art for waste heat recovery, geothermal power, and biomass power applications and is promising in the development of new SPT and heat battery systems. It can serve as a bottom cycle for SRC [28] and supercritical carbon dioxide Brayton cycle [29], or be integrated with tower-concentrating photovoltaic technology [30]. Common ORC fluids are refrigerants, hydrocarbons, and siloxanes with operating temperatures below 300 °C.

In the proposed system, the ORC fluid is a high-temperature biphenyl-diphenyl oxide (BDO) mixture. It absorbs heat from the molten salts, evaporates at about 400 °C, expands in the turbine, and releases heat to the bottom SRC for water preheating and steam generation. The eutectic mixture, consisting of 26.5% biphenyl and 73.5% diphenyl oxide, has significant potential in high-temperature ORC [31,32] and cascade cycle applications [33]. It can work in liquid, binary phase, and vapor states. The BDO mixture has more familiar commercial names of Therminol® VP-1, Dowtherm-A, or Diphyl [34]. Nowadays, it is a widely-used heat transfer medium in PTC plants up to 400 °C [34,35]. Its excellent thermal and chemical stability was demonstrated by repeated experiments in a closed boiler loop [36] and heat pipes [37]. The BDO mixture was successfully applied as the top cycle fluid of a binary cycle in a radioisotope heater unit as early as 1971. The system operated continuously with an overall efficiency of 8.5% and an output of 680 W [38]. The BDO mixture seemed to be a favorable bottom cycle fluid in a binary liquid metal-ORC distributed system [34]. The potential of the ORC using the BDO mixture for cogeneration in the waste heat recovery application was also explored [39].

To the authors' best knowledge, an SRC topped by an ORC for SPT and heat battery applications has yet to be reported. In the literature, cascade liquid metal-SRC for concentrated solar power generation [40] and cascade ORC-SRC for waste heat recovery using gas fumes to heat the organic fluids and water sequentially [39] have been reported. The ORC-SRC incorporated by two-tank molten salts is original. As a first-of-its-kind system, its thermo-economic performance is unknown. Unlike common cascade cycles where the bottom cycle gets all the heat from the top one, the ORC-SRC in this paper is a partial cascade cycle. The bottom SRC gets some heat from the ORC for preheating and evaporating and the rest heat from the molten salts for superheating and reheating. The proposed ORC-SRC may have a higher thermal efficiency than the traditional SRC-based SPT and heat battery plants. The operating principles and characteristics of the novel system are elaborated. Mathematical models are built, followed by thermodynamic optimization on the water evaporation temperature. The irreversible losses in the turbines, main heat exchangers, and pumps are analyzed. Finally, the equivalent payback period for the additional investment on the ORC is evaluated.

2. Description of the system

Fig. 1 shows the schematic diagram of the novel partial cascade ORC-SRC system (i.e., System I). A solar tower receiver is taken as an example. The heat source can be replaced by an electrical heater or heat pump in heat batteries. The ORC-SRC is the same in both CSP and heat battery applications. It consists of three loops: the molten salt cycle in red, the top ORC in blue, and the bottom SRC in black. The components of each subcycle and the operating principles of the system are described as follows.

The molten salt circuit is composed of a solar thermal central receiver, a high-temperature tank (HTT), and a low-temperature tank (LTT). The hot molten salts from the outlet of the HTT flow through three paths. The first loop heats the evaporator and preheater of the ORC in succession. The remaining two branches heat the superheater and reheater of the SRC, respectively.

The top cycle includes an ORC turbine, an internal heat exchanger (IHX), an ORC preheater, and an ORC evaporator. The superheated vapor at the outlet of the ORC turbine releases heat through the IHX, steam generator, and steam preheater in turn. Then the saturated liquid BDO mixture is consecutively pumped to the IHX, ORC preheater, and evaporator through P3. The saturated vapor from the outlet of the ORC evaporator drives the ORC turbine.

The SRC mainly comprises the steam preheater, generator, superheater, reheater, high-pressure (HP) and low-pressure (LP) turbines, and condenser. Two extractions, 11 and 12, are taken from the HP turbine to

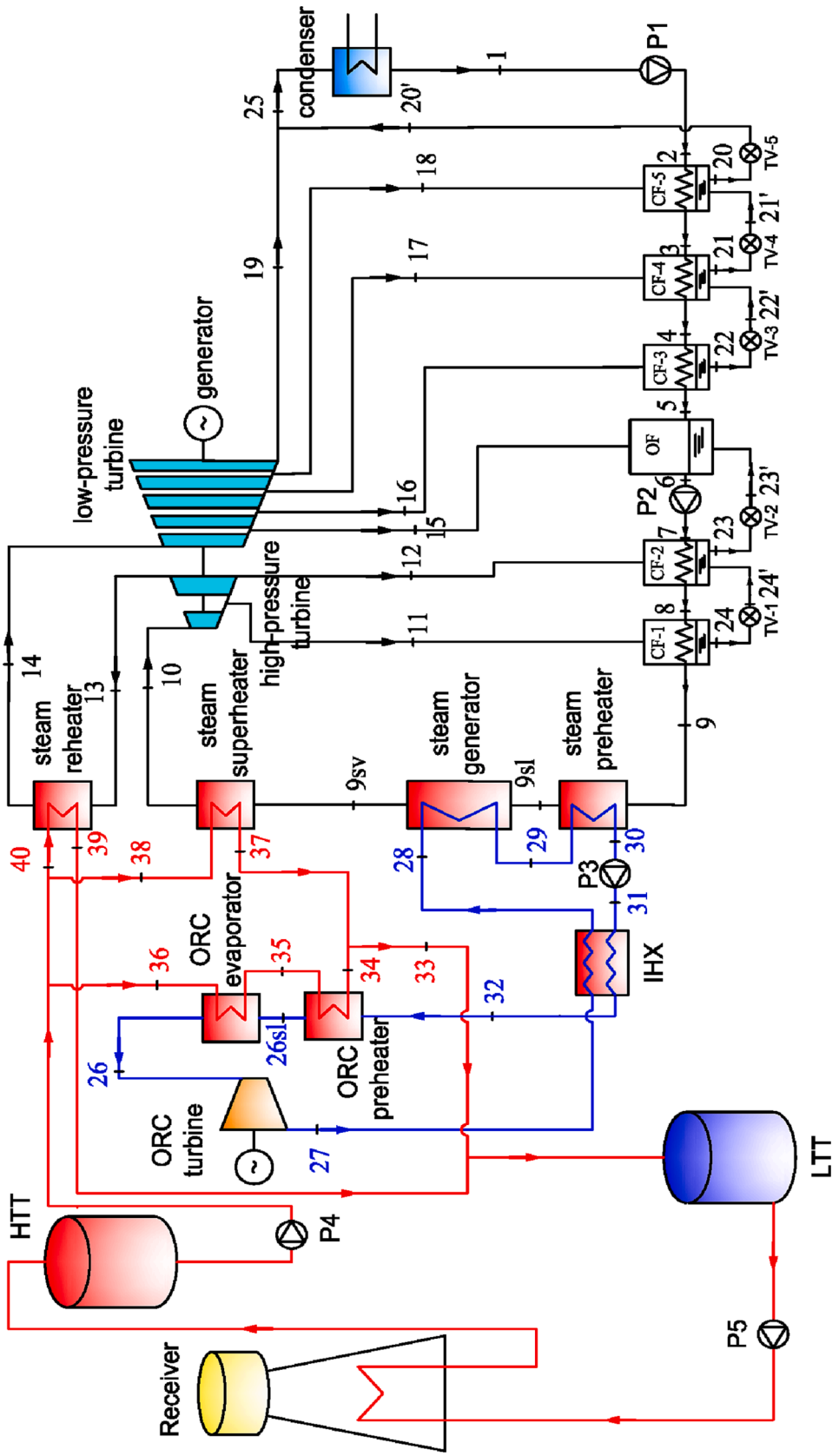

Fig. 1. Schematic diagram of System I.

the closed feedwaters (CF-1, CF-2). The closed feedwater heaters are shell-and-tube-type recuperators used to increase the feedwater temperature by condensing the extracted steam. Four extractions, 15–18, are bled to a deaerator (open feedwater, OF) and three closed feedwaters (CF-3, CF-4, CF-5) from the LP turbine. A deaerator is a direct contact-type heat exchanger in which streams at different temperatures are mixed to form a stream at an intermediate temperature. It is also used for removing air and other dissolved gases which can cause corrosion problems.

The ORC can be used only for water evaporation without preheating (System II), as displayed in Fig. 2. System II is similar to System I in structure. The difference is that the middle branch of the molten salts in System II is first used to heat the steam superheater and then merges with the first branch to heat the steam preheater. By comparison, the middle branch merely provides heat for the steam superheater in System I.

3. Mathematical models

Subcritical cycles are considered for the partial cascade ORC-SRC. The *T-s* diagram of System I is illustrated in Fig. 3. The BDO mixture is a dry ORC fluid and remains superheated during expansion. Incomplete saturated liquid and saturated vapor curves are displayed. The reason is that the available thermophysical property data of the mixture provided by the manufacturer are in the temperature range of up to 420 °C, which is far below its pseudocritical temperature of 499 °C [41].

3.1. Thermodynamics

This paper focuses on System I, with a brief comparison with System II in Section 4.3. The thermodynamic states (1–40) of System I are marked in Fig. 1. The equations for heat transfer, power conversion, and exergy analysis are presented below.

3.1.1. Heat exchangers

The heat balance in the steam preheater, steam generator and IHX is calculated as

$$q_{st,pre} = m_{ORC}(h_{29} - h_{30}) = m_9(h_{9sl} - h_9) \tag{1}$$

$$q_{st,g} = m_{ORC}(h_{28} - h_{29}) = m_9(h_{9sv} - h_{9sl}) \tag{2}$$

$$q_{IHX} = h_{27} - h_{28} = h_{32} - h_{31} \tag{3}$$

where the subscripts *sl* and *sv* denote saturated liquid and saturated vapor, respectively.

The physical properties of molten salts can be calculated according to the formulas in Table 2. The heat balance in the steam reheater, steam superheater, ORC evaporator, and ORC preheater is determined by

$$q_{st,re} = m_{40}\int_{t_{39}}^{t_{40}} c_p dt = m_{13}(h_{14} - h_{13}) \tag{4}$$

$$q_{st,sup} = m_{38}\int_{t_{37}}^{t_{38}} c_p dt = m_{10}(h_{10} - h_{9sv}) \tag{5}$$

$$q_{ORC,evap} = m_{36}\int_{t_{35}}^{t_{36}} c_p dt = m_{ORC}(h_{26} - h_{26sl}) \tag{6}$$

$$q_{ORC,pre} = m_{36}\int_{t_{34}}^{t_{35}} c_p dt = m_{ORC}(h_{26sl} - h_{32}) \tag{7}$$

The minimum temperature difference (Δt_{min}) occurs at the outlet of molten salts for the steam reheater, steam superheater, and ORC perheater. In contrast, Δt_{min} takes place at the pinch point for the steam preheater.

$$t_{39} - t_{13} = t_{37} - t_{9sv} = t_{34} - t_{32} = t_{29} - t_{9sl} = \Delta t_{min} \tag{8}$$

The IHX effectiveness (ε_{IHX}) is expressed by

$$\varepsilon_{IHX} = \frac{h_{27} - h_{28}}{h_{27} - h(t_{31}, p_{28})} \tag{9}$$

where $h(t_{31}, p_{28})$ is the specific enthalpy of the BDO mixture at the pump's outlet temperature of t_{31} and the condensing pressure of p_{28}. This would be the theoretical lowest enthalpy to which the hot stream could be cooled down. As $t_{30} = t_{28sv}$, $p_{28sv} = p_{28}$, and the liquid temperature increment after pressurization is limited, $h(t_{31}, p_{28})$ can be regarded as the saturated vapor enthalpy at t_{31}. The deduction of h_{27} and t_{28} will be given in Sections 3.1.6 and 4.2.1, respectively. Then t_{31} and h_{28} can be obtained from Eqs. (8) and (9) successively.

The terminal temperature difference, which is the difference between the saturation temperature of the extraction steam and the feedwater outlet temperature, is set at 1.5 °C [43].

$$t_{sv@p11} - t_9 = t_{sv@p12} - t_8 = t_{sv@p15} - t_6 = t_{sv@p16} - t_5 = t_{sv@p17} - t_4 = t_{sv@p18} - t_3 = \tag{10}$$

The drain cooler approach, which is the difference between the drain outlet temperature and the feedwater inlet temperature, is set at 5 °C [43].

$$t_{24} - t_8 = t_{23} - t_7 = t_{22} - t_4 = t_{21} - t_3 = t_{20} - t_2 = \tag{11}$$

The heat balance in CF-1 and CF-2 is defined as

$$m_{11}(h_{11} - h_{24}) = m_9(h_9 - h_8) \tag{12}$$

$$m_{12}h_{12} + m_{24}h_{24'} + m_7h_7 = m_8h_8 + m_{23}h_{23} \tag{13}$$

The same is true for OF, CF-3, CF-4 and CF-5.

The condensed steam is throttled by throttle valves and flows into the neighboring feedwaters. The enthalpy of water after throttling is equal to that before throttling, $h_{24'} = h_{24}$, $h_{23'} = h_{23}$, $h_{22'} = h_{22}$, $h_{21'} = h_{21}$.

The pressure drop in feed water extraction lines usually ranges from 2.5% to 3.5%. In this study, the pressure drop is set at 3%.

3.1.2. Low temperature tank temperature

According to the conservation of mass and energy

$$m_{33} = m_{34} + m_{37} \tag{14}$$

$$t_{33} = \frac{m_{34}t_{34} + m_{37}t_{37}}{m_{33}} \tag{15}$$

where $m_{34} = m_{36}$, $m_{37} = m_{38}$, $m_{39} = m_{40}$. The LTT temperature is obtained by

$$t_{LTT} = \frac{m_{33}t_{33} + m_{39}t_{39}}{m_{33} + m_{39}} \tag{16}$$

3.1.3. Turbines

The work produced by the HP and LP turbines is given as

$$w_{HT} = m_{10}h_{10} - m_{11}h_{11} - m_{12}h_{12} - m_{13}h_{13} \tag{17}$$

$$w_{LT} = m_{14}h_{14} - m_{15}h_{15} - m_{16}h_{16} - m_{17}h_{17} - m_{18}h_{18} - m_{19}h_{19} \tag{18}$$

The specific enthalpy of each extraction can be obtained by the isentropic efficiencies of HP and LP turbines

$$\varepsilon_{HT} = \frac{h_{10} - h_{11}}{h_{10} - h_{11s}} = \frac{h_{11} - h_{12}}{h_{11} - h_{12s}} \tag{19}$$

$$\varepsilon_{LT} = \frac{h_{14} - h_{15}}{h_{14} - h_{15s}} = \frac{h_{15} - h_{16}}{h_{15} - h_{16s}} = \frac{h_{16} - h_{17}}{h_{16} - h_{17s}} = \frac{h_{17} - h_{18}}{h_{17} - h_{18s}} = \frac{h_{18} - h_{19}}{h_{18} - h_{19s}} \tag{20}$$

where *s* stands for isentropic.

The steam at the last stage of the LP turbine outlet is usually wet steam. ε_{LT} is associated with steam wetness, as described by the Bau-

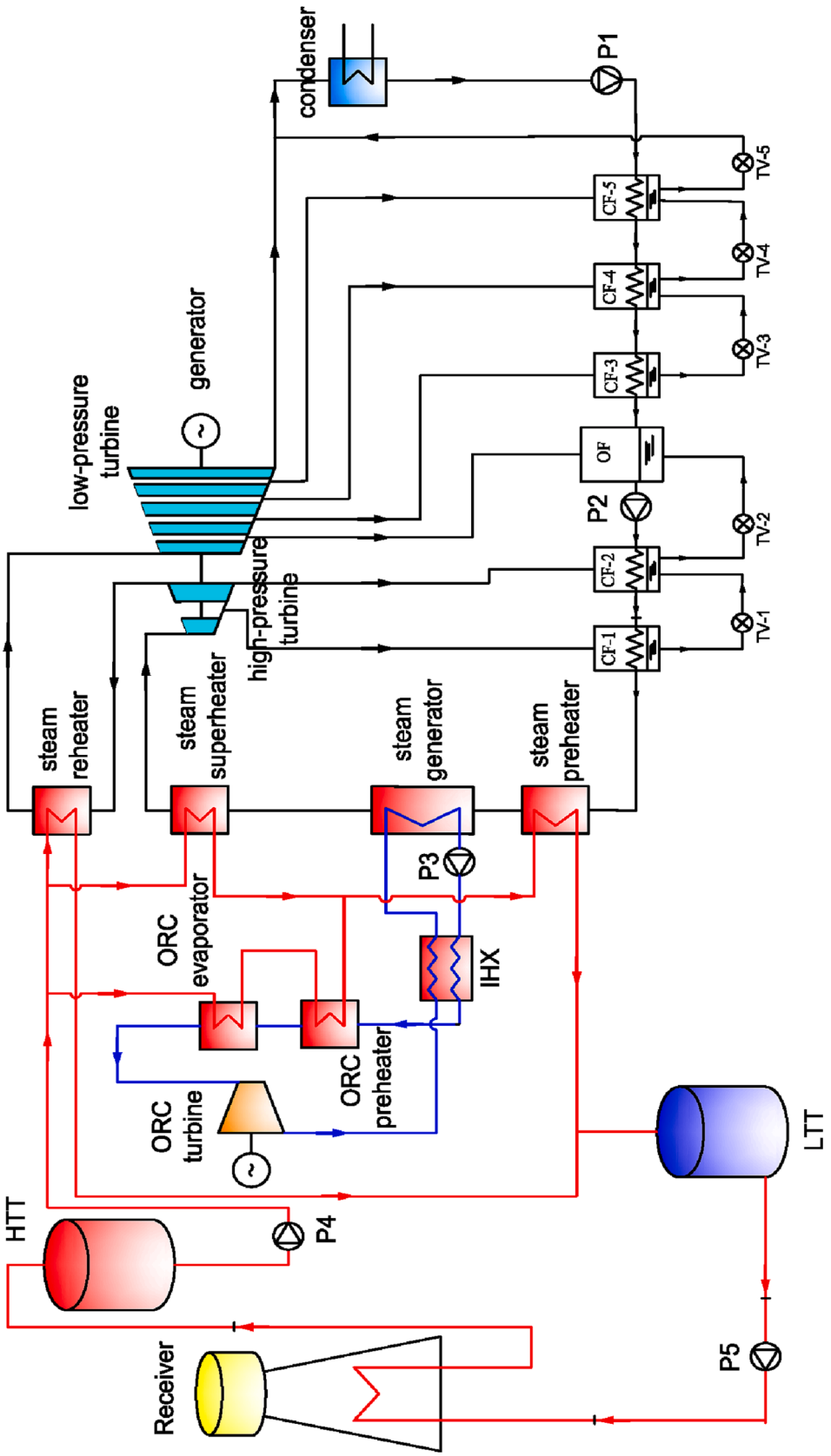

Fig. 2. Schematic diagram of System II.

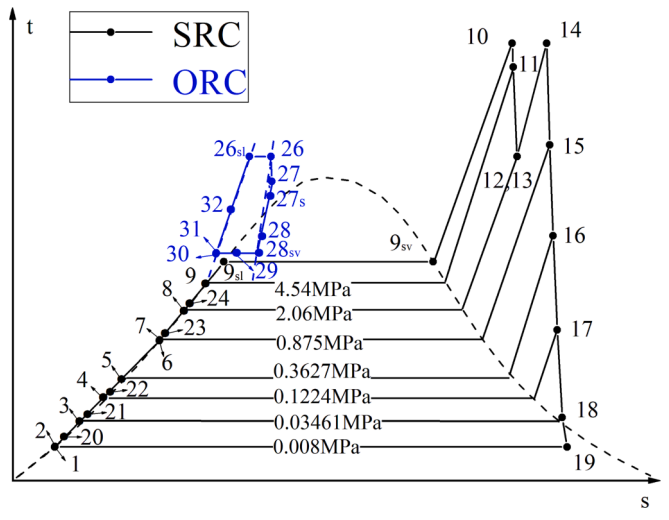

Fig. 3. *T-s* diagram of the novel system.

Table 2
The physical properties of molten salts [23,42].

Parameters	Formulas
Density (kg/m^3)	$\rho_{ms} = -0.636t + 2090$
Specific heat capacity (J/kg·°C)	$c_{p_{ms}} = 0.172t + 1443$
Thermal conductivity (W/m·°C)	$\lambda_{ms} = 0.443 + 1.9 \times 10^{-4}t$
Dynamic viscosity (mPa·s)	$\mu_{ms} = 22.714 - 0.12t + 2.281 \times 10^{-4}t^2 - 1.474 \times 10^{-7}t^3$

mann rule, which is a longstanding empirical rule in the history of turbomachinery [44,45].

$$\varepsilon_{LT} = \varepsilon_{LT,sh}(1 - ay_{av}) \tag{21}$$

$$y_{av} = (y_{14} + y_{19})/2 \tag{22}$$

where $\varepsilon_{LT,sh}$ is the reference isentropic efficiency assuming that the LP turbine works with superheated steam; a is an empirical coefficient known as the Baumann factor, which is usually assumed to be 1.0 [45]; and y_{14} and y_{19} are respectively the main steam and exhaust steam wetness. For the HP steam turbine, a higher inlet pressure leads to greater steam density, smaller volume flow rate, less nozzle flow passage area and lower specific speed. The corresponding nozzle and moving blade losses, blade height loss, leakage loss, impeller friction loss, and other losses have negative effects on the performance, and finally result in lower isentropic efficiency.

For the ORC turbine,

$$w_{OT} = m_{ORC}(h_{26} - h_{27}) = m_{ORC}(h_{26} - h_{27s})\varepsilon_{OT} \tag{23}$$

where ε_{OT} denotes the ORC turbine efficiency.

3.1.4. Pumps

The work consumed by P1, P2 and P3 is calculated by

$$w_{P1} = m_1(h_2 - h_1) = m_1(h_{2s} - h_1)/\varepsilon_P \tag{24}$$

$$w_{P2} = m_9(h_7 - h_6) = m_9(h_{7s} - h_6)/\varepsilon_P \tag{25}$$

$$w_{P3} = m_{ORC}(h_{31} - h_{30}) = m_{ORC}(h_{31s} - h_{30})/\varepsilon_P \tag{26}$$

where ε_P is the pump efficiency.

3.1.5. Entropy of the mixture in a saturated state

The datasheet of Therminol® VP-1 (a brand of BDO mixture) supplied by Eastman Corp is employed in this paper for the thermophysical properties. The saturation state parameters at intervals of 10 °C are available [41]. Eastman Corp provides high-performance fluids backed by expert technical support and a strong foundation of more than 50 years in the industry and used in more than 15,000 systems across the globe [46]. The parameters (like *T, p, h, v*) in a saturated state at variable temperature can be calculated by linear interpolation.

The manufacturer's datasheet provides the enthalpies of saturated liquid and vapor, together with the temperatures, pressures, and densities (i.e., specific volumes). The entropy is not provided, but it can be derived from the thermodynamic relation.

$$dh = Tds + vdp \tag{27}$$

As entropy or specific entropy is a state parameter, the selection of the reference state will not affect the thermodynamic performance of the ORC. The isentropic efficiencies of the turbines are related to the variation of entropy rather than the absolute value. It is assumed that the saturation entropy of liquid BDO mixture at 313.34 °C ($s_{313.34^\circ C,\,sl}$) is 3 kJ/kg·K, which is consistent with the hypothesis in the authors' previous work [47].

3.1.6. Enthalpies of the mixture in a superheated state

The enthalpy of BDO mixture in a superheated state is not provided in the manufacturer's datasheet. The information is generally necessary in modelling the ORC efficiency. As shown in Eq. (23), h_{27} is required to calculate w_{OT}, which is beyond the saturation vapor curve. It is difficult to apply a conventional ORC efficiency model without thermodynamic parameters at the superheated state. To overcome this problem, the authors have developed an ORC efficiency model based on the equivalent hot side temperature (T_{EHST}) [48], in which only the saturated parameters are required.

$$T_{EHST} \approx \frac{h_{26} - h_{30} - v_{30}(p_{26} - p_{30})}{s_{26} - s_{30}} \tag{28}$$

The efficiency of ORC in a basic structure ($\eta_{ORC,b}$) without an IHX can be built with the assistance of T_{EHST}. $\eta_{ORC,b}$ is in good agreement with the actual. The relative error ranges from −0.7% to 3.4% on the use of 27 fluids [48].

$$\eta_{ORC,b} = \left(1 - \frac{T_{30}}{T_{EHST}}\right) \bullet \frac{\varepsilon_{OT} \bullet \varepsilon_g + v_{30}(p_{26} - p_{30})/\left(\varepsilon_P \bullet \int_{26}^{28sv} v_{sv}dp\right)}{1 + v_{30}(p_{26} - p_{30})/\left(\int_{26}^{28sv} v_{sv}dp\right)} \tag{29}$$

where $\int_{26}^{28sv} v_{sv}dp$ can be obtained by piecewise integration and then summation.

$$\int_{26}^{28sv} v_{sv}dp = \int_{400}^{390} v_{sv}dp + \int_{390}^{380} v_{sv}dp + \int_{380}^{370} v_{sv}dp + \cdots + \int_{330}^{320} v_{sv}dp \tag{30}$$

Meanwhile, $\eta_{ORC,b}$ can be estimated as

$$\eta_{ORC,b} = \frac{(h_{26} - h_{27}) \bullet \varepsilon_g - (h_{31} - h_{30})}{h_{26} - h_{31}} \tag{31}$$

Most ORC fluids at liquid state are not compressible, and most of the heat is taken out by the condensation process [48]. Therefore

$$h_{31s} \approx h_{30} + v_{30}(p_{31s} - p_{30}) \tag{32}$$

where $p_{31s} = p_{31} = p_{32} = p_{26}$ (p_{26} is 1.09 MPa assuming that t_{26} is 400 °C [41]). p_{30}, h_{30} and v_{30} can be obtained by linear interpolation. h_{27} can be deduced by combining Eqs. (26) and (28–32) as the ideal power output is determined by the heat input and ORC efficiency.

With the heat recovered from the IHX ($m_{ORC}(h_{32} - h_{31})$) and the power output of a basic ORC, the efficiency of the ORC with the IHX can be deduced as follows.

3.1.7. Thermal efficiency

The thermal efficiency of the SRC can be appraised by

$$\eta_{SRC} = \frac{w_{SRC}}{q_{SRC}} = \frac{(w_{HT} + w_{LT}) \bullet \varepsilon_g - w_{P1} - w_{P2}}{m_9(h_{10} - h_9) + m_{13}(h_{14} - h_{13})} \tag{33}$$

The thermal efficiency of the ORC using BDO mixture is derived from

$$\eta_{ORC} = \frac{w_{ORC}}{m_{ORC}(h_{26} - h_{32})} = \frac{w_{OT} \bullet \varepsilon_g - w_{P3}}{m_{ORC}(h_{26} - h_{32})} \tag{34}$$

The heat to power conversion efficiency of the ORC-SRC is calculated as

$$\eta_{ORC-SRC} = \frac{w_{ORC-SRC}}{q_{ORC-SRC}} = \frac{w_{ORC}+w_{SRC}}{m_{10}(h_{10} - h_{9_{sv}}) + m_{13}(h_{14} - h_{13}) + m_{ORC}(h_{26} - h_{32})} \tag{35}$$

3.1.8. Entropy generation and exergy destruction

Entropy generation (ΔS) represents the thermodynamic irreversibility in the components, and $T_a \Delta S$ equals the exergy loss, which is indexed in Table 3 [49].

3.1.9. Exergy efficiency

Exergy efficiency is an important index to evaluate the perfection of thermodynamics. The theoretical framework for the exergy analysis presented by Xu et. al is employed [50]. The exergy absorbed by the BDO mixture is expressed by

$$Ex_{ORC} = m_{ORC}[h_{26} - h_{32} - T_a(s_{26} - s_{32})] \tag{36}$$

The exergy absorbed by the steam is defined by

$$Ex_{SRC} = m_{13}[h_{14} - h_{13} - T_a(s_{14} - s_{13})] + m_{10}[h_{10} - h_{9_{sv}} - T_a(s_{10} - s_{9_{sv}})] \tag{37}$$

The exergy consumed by the ORC-SRC is

$$Ex_{ORC-SRC} = Ex_{ORC} + Ex_{SRC} \tag{38}$$

The exergy efficiencies of the SRC and ORC-SRC are separately estimated as

$$\eta_{ex,SRC} = \frac{w_{SRC}}{Ex_{SRC}} \tag{39}$$

$$\eta_{ex,ORC-SRC} = \frac{w_{ORC-SRC}}{Ex_{ORC-SRC}} \tag{40}$$

3.2. Thermo-economics

An evaluation of the cost and payback time of the entire system is not conducted due to its complexity. Instead, an operational demonstration project SUPCON Delingha 50 MWe Tower [11,51] is taken as a reference. The economic advantages of System I will be derived by comparing the performance before and after introducing the BDO mixture-based ORC in the reference. Excess electricity per year can be achieved at the expense of additional ORC investment. An equivalent payback period (*EPP*) with respect to the extra ORC can be given by

$$EPP = \frac{C_{add}}{Y} \tag{41}$$

where C_{add} is the added cost for the ORC employment, and Y is the excess annual electricity yield.

The total annual power output of a solar power system consists of two parts: the rated working mode when the solar irradiation is sufficient and the discharge mode when the irradiation is insufficient. As the efficiency of an SPT plant (η_{SPT}) in the rated condition can be approximately defined as the product of the efficiencies of three main subsystems, namely, heliostat field (η_{field}), receiver (η_{rec}), and power cycle (η_{pc}) [52]. η_{pc} remains constant in the two modes for a given dual-tank SPT system while η_{field} and η_{rec} vary hourly with the geographical location and environmental factors such as the radiation intensity, ambient temperature, wind speed, solar azimuth and altitude, etc. As a result, η_{SPT} also varies hourly, which then affects the power output in the rated mode. For the convenience of calculation, it is assumed that the heliostats and receiver are kept constant after adding ORC in the reference project. In other words, the introduction of ORC has no effect on the hourly η_{field} or η_{rec}. The annual heat obtained (Q_{ann}) by the solar island is thus unchanged. The annual power output (W) is the the product of Q_{ann} and η_{pc}, and η_{pc} is constant for a given power cycle. In this way, the extra annual power generation by System I is simply attributed to the improvement in η_{pc}. η_{pc} is raised from the reference SRC efficiency ($\eta_{SRC,ref}$) to $\eta_{ORC-SRC}$. The computational procedure is presented in Fig. 4. Determining the annual electricity output of System I is reasonable by

$$W_{SystemI} = W_{ref} \times \frac{\eta_{ORC-SRC}}{\eta_{SRC,ref}} \tag{42}$$

C_{add} includes the investments in IHX, ORC preheater, ORC evaporator, ORC turbine, P3, ORC generator, extra molten salts and BDO mixture. Determining the *EPP* is reasonable by

$$EPP = \frac{C_{IHX} + C_{ORC,pre} + C_{ORC,evap} + C_{OT}+C_{P3} + C_{ORC,g} + C_{ms,extra} + C_{BDO}}{Y_{SystemI} - Y_{ref}} \tag{43}$$

3.2.1. Cost of supplementary heat exchangers

The purchased cost of a heat exchanger is [53]

$$log_{10}C_P = K_1 + K_2 log_{10}A + K_3(log_{10}A)^2 \tag{44}$$

where C_P is a basic cost concerning the heat exchanger area. Considering the specific material of the construction and operating pressure, the bare module cost for a heat exchanger should be corrected as [53]

$$C_{BM} = C_P(B_1 + B_2F_MF_P) \tag{45}$$

C_{BM} is the corrected cost, F_M is the material correction factor, and F_P is a measure that reflects the pressure factor since the system components work at a pressure much higher than the ambient pressure, which is determined by [53]

$$log_{10}F_P = C_1 + C_2 log_{10}(10p - 1) + C_3[log_{10}(10p - 1)]^2 \tag{46}$$

K_1, K_2, K_3, B_1, B_2, C_1, C_2 and C_3 are coefficients for the cost evaluation of components. The values are posted in Table 4. Since the unit in the parentheses of the second term on the right side of Eq. (46) is gage pressure in bar, a transformation from MPa to bar is thus needed to fit the equation.

The actual cost needs to be converted from the cost of 2001 by introducing the Chemical Engineering Plant Cost Index (*CEPCI*) [55]. The cost of 2018 should be corrected as

$$C_{BM,2018} = C_{BM,2001} \bullet CEPCI_{2018}/CEPCI_{2001} \tag{47}$$

where $CEPCI_{2001} = 397$, $CEPCI_{2018} = 648.7$.

Table 3
Definition of the exergy destruction in the components [49].

Components	Exergy destruction
HP turbine	$T_a(m_{11}s_{11} + m_{12}s_{12} + m_{13}s_{13} - m_{10}s_{10})$
LP turbine	$T_a(m_{15}s_{15} + m_{16}s_{16} + m_{17}s_{17} + m_{18}s_{18} + m_{19}s_{19} - m_{14}s_{14})$
ORC turbine	$T_a m_{ORC}(s_{27} - s_{26})$
steam reheater	$T_a(m_{14}s_{14} + m_{39}s_{39} - m_{40}s_{40} - m_{13}s_{13})$
steam superheater	$T_a(m_{37}s_{37} + m_{10}s_{10} - m_{38}s_{38} - m_9 s_{9sv})$
steam generator	$T_a(m_{ORC}s_{29} + m_9 s_{9sv} - m_{ORC}s_{28} - m_9 s_{9sl})$
steam preheater	$T_a(m_{ORC}s_{30} + m_9 s_{9sl} - m_{ORC}s_{29} - m_9 s_9)$
ORC evaporator	$T_a(m_{35}s_{35} + m_{ORC}s_{26} - m_{36}s_{36} - m_{ORC}s_{26sl})$
ORC preheater	$T_a(m_{34}s_{34} + m_{ORC}s_{26sl} - m_{35}s_{35} - m_{ORC}s_{32})$
IHX	$T_a m_{ORC}(s_{32} + s_{28} - s_{27} - s_{31})$
condenser	$T_a m_1[s_1 - s_{25} - (h_1 - h_{25})/T_a]$
P1	$T_a m_1(s_2 - s_1)$
P2	$T_a m_6(s_7 - s_6)$
P3	$T_a m_{ORC}(s_{31} - s_{30})$

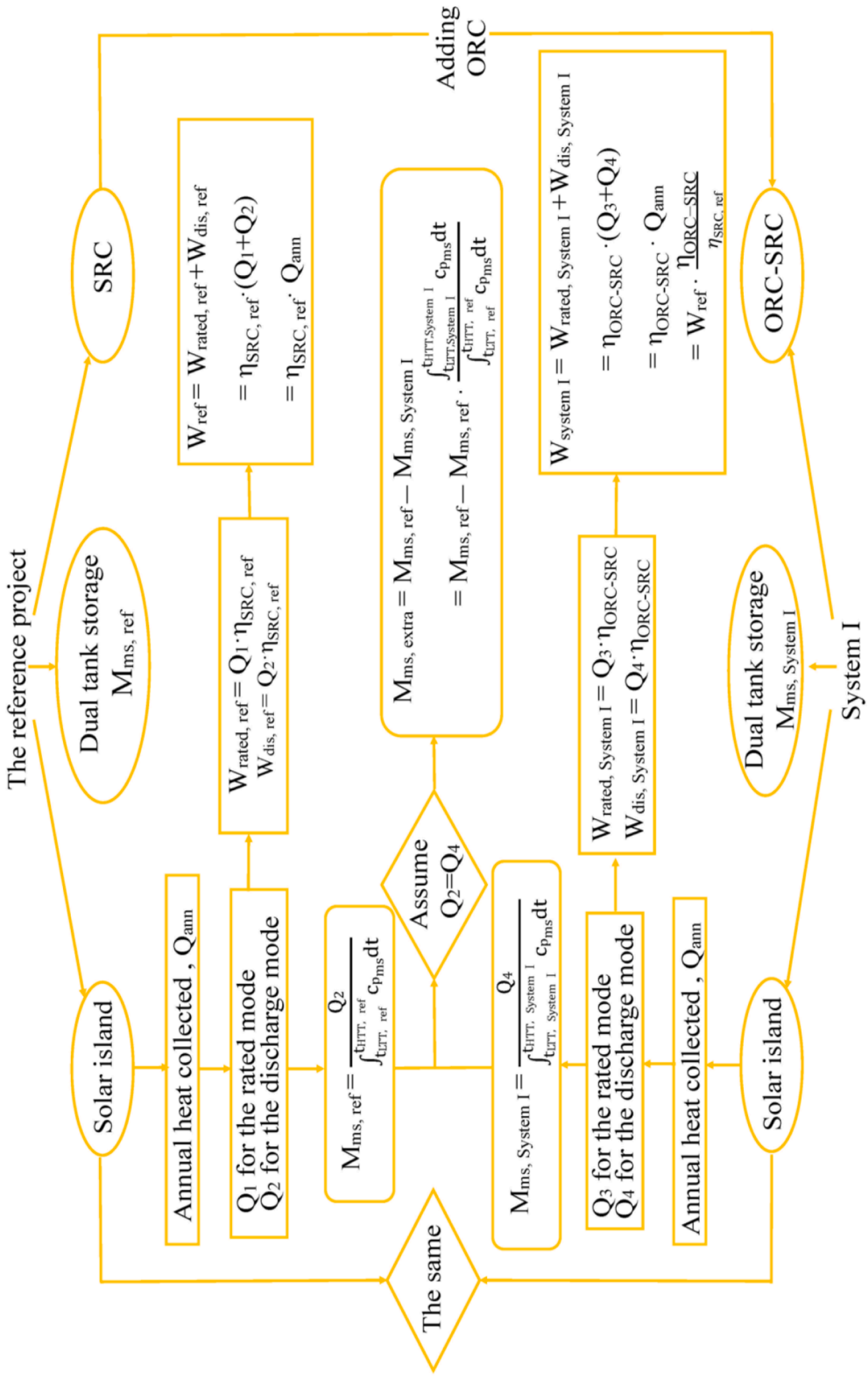

Fig. 4. Calculation procedure of $W_{SystemI}$ and $M_{ms,extra}$.

3.2.2. Cost of organic Rankine cycle turbine, generator and P3

The purchased cost of the turbine and pump is [53]

$$log_{10}C_P = K_1 + K_2 log_{10}w + K_3 (log_{10}w)^2 \quad (48)$$

where C_P is a basic cost concerning the work output or consumption. The bare module cost of the pump is calculated by Eq. (45) [53]. The bare module cost of the ORC turbine is [53]

$$C_{OT} = C_{BM,OT} = C_P F_{BM} F_P \quad (49)$$

The cost of the ORC generator is [56]

$$C_{ORC,g} = 60(\varepsilon_g w_{OT})^{0.95} \quad (50)$$

Table 4
Values of constants for different components [54].

Equipment	IHX / ORC preheater / ORC evaporator	Pump	Turbine
K_1	4.3247	3.3892	2.7051
K_2	−0.3030	0.0536	1.4398
K_3	0.1634	0.1538	−0.1776
C_1	0.0388	−0.3935	0
C_2	−0.11272	0.3957	0
C_3	0.08183	−0.00226	0
B_1	1.63	1.89	/
B_2	1.66	1.35	/
F_M	1.40	1.60	/
F_{BM}	/	/	3.40

3.2.3. Cost of molten salts

As disclosed in Section 3.2, Q_{ann} remains the same for the reference project after introducing the ORC. At the same time, the change in the proportion of Q_{ann} allocated to the rated and discharge conditions does not affect W. For the sake of simplicity, it is reasonable to assume that the proportions of Q_{ann} allocated to the two modes remain constant separately after operating the ORC, as depicted in Fig. 4. The required mass of molten salts for System I can thus be deduced by

$$M_{ms,System\text{I}} = M_{ms,ref} \bullet \frac{\int_{t_{LTT,System\text{I}}}^{t_{HTT,System\text{I}}} c_{p,ms}dt}{\int_{t_{LTT,ref}}^{t_{HTT,ref}} c_{p,ms}dt} \tag{51}$$

where $M_{ms,System\text{I}}$ and $M_{ms,ref}$ represent the molten salts mass of System I and the reference, respectively.

The cost of extra molten salts is

$$C_{ms,extra} = P_{ms} \bullet M_{ms,extra} = P_{ms} \bullet (M_{ms,System\text{I}} - M_{ms,ref}) \tag{52}$$

where P_{ms} represents the molten salts price, and it is 0.5 $/kg [57].

3.2.4. Cost of the mixture

It is difficult to accurately estimate the amount of working fluid charged for an ORC system because the report on this aspect is rare. The filling mass is 5.57 kg and 5.4 kg for a 1-kWe power output generated by the turbine according to the literature [58,59]. The required BDO mixture mass (M_{BDO}) is proportional to $w_{OT} \bullet \varepsilon_g$ and the cost of the BDO mixture can be deduced by

$$C_{BDO} = P_{BDO} \times M_{BDO} \tag{53}$$

where P_{BDO} is the BDO mixture price, and it is 2.2 $/kg [57].

3.2.5. Annual revenues

The annual yield is the product of electricity price and annual electricity output

$$Y_{system\text{I}} = P_e \bullet W_{System\text{I}} \tag{54}$$

$$Y_{ref} = P_e \bullet W_{ref} \tag{55}$$

where P_e is the electricity price, and it is 0.184 $/kWh [60].

4. Results and discussion

Specific parameters for the performance prediction are listed in Table 5. The SRC evaporation temperature (t_{9sv}) is a crucial parameter because it not only affects the ORC efficiency (η_{ORC}) and SRC efficiency (η_{SRC}), but also influences the ORC-SRC efficiency ($\eta_{ORC-SRC}$). In this simulation, t_{9sv} ranges from 260 °C to 350 °C in the following considerations. First, the minimum inlet steam pressure (p_{10}) is theoretically higher than the first stage suction pressure (p_{11}) of 4.54 MPa (the corresponding saturation temperature is 257.98 °C). The lower limit of t_{9sv} is chosen as 260 °C. The simulation below will also show that t_{9sv} corresponding to the maximum $\eta_{ORC-SRC}$ is not lower than 260 °C. Second, the maximum operating pressures of current SPT plants generally do not exceed 16 MPa [23] (the corresponding saturation temperature is 347.35 °C). The upper limit of t_{9sv} is selected as 350 °C. The temperature interval for t_{9sv} is 1 °C in the calculation.

Table 5
Specific parameters for calculation.

Term	Value
Gross electric power of SRC [61],$(w_{HT}+w_{LT}) \bullet \varepsilon_g$	50 MWe
HP turbine efficiency [61,62],ε_{HT}	0.855
LP turbine efficiency [61,62],ε_{LT}	0.895
Pressure of extraction no. 1 [62],p_{11}	4.54 MPa
Pressure of extraction no. 2 [62],p_{12}	2.06 MPa
Pressure of extraction no. 3 [62],p_{15}	0.875 MPa
Pressure of extraction no. 4 [62],p_{16}	0.3627 MPa
Pressure of extraction no. 5 [62],p_{17}	0.1224 MPa
Pressure of extraction no. 6 [62],p_{18}	0.03461 MPa
Steam condensation pressure [62],p_{19}	0.008 MPa
Pressure drop in feed water extractions lines [43]	3%
HP turbine inlet temperature [22],t_{10}	540 °C
ORC turbine inlet temperature [63],t_{26}	400 °C
HTT temperature [50],t_{HTT}	565 °C
Minimum heat transfer temperature difference [63],Δt_{min}	10 °C
ORC turbine efficiency [63],ε_{OT}	0.87
Generator efficiency [60],ε_g	0.95
Pump efficiency [64],ε_P	0.75
IHX effectiveness [64],ε_{IHX}	0.8
Standard ambient temperature [64],t_a	25 °C

4.1. Thermodynamic performance analysis

System I is exemplified. The heat-to-power conversion efficiency is optimized, followed by an investigation on the mass flow rate, power output, heat transfer in heat exchangers, and exergy performance at different SRC evaporation temperatures.

4.1.1. Heat-to-power conversion efficiency

Variations of η_{ORC}, η_{SRC} and $\eta_{ORC-SRC}$ are exhibited in Fig. 5. Given the HTT temperature (t_{HTT}) and the steam condensation pressure (p_{19}), the equivalent hot side temperature for the SRC and the equivalent cold side temperature for the ORC increase as t_{9sv} rises, resulting in increasing η_{SRC} and declining η_{ORC}. $\eta_{ORC-SRC}$ is a compromise between η_{ORC} and η_{SRC}. Thermodynamic parameters of each state point at the optimal condition are displayed in Table 6. Notably, the optimal t_{9sv} for System I is about 290 °C, which is beneficial for the HP turbine design as the corresponding p_{10} of 7.44 MPa is lower than those of the recent molten salts SPT plants (11–16 MPa). It can reduce leakage loss through the HP turbine and offer a higher turbine efficiency. It also enables the use of

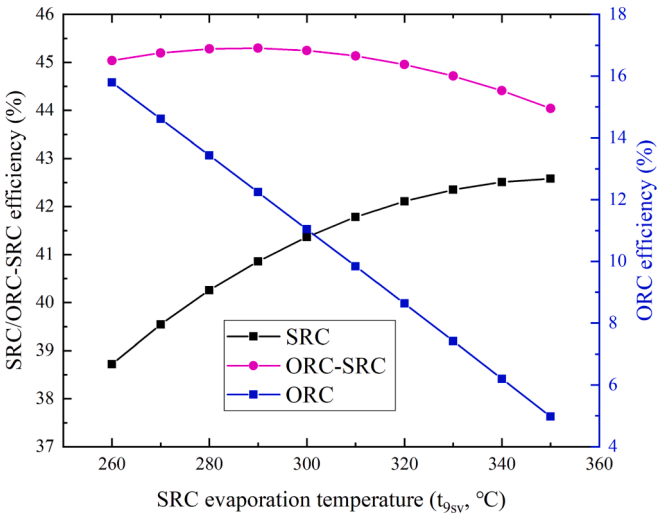

Fig. 5. Variations of SRC, ORC and ORC-SRC efficiencies.

Table 6
Thermodynamic parameters of each state point at the optimal condition.

State point	Temperature (°C)	Pressure (MPa)	Enthalpy (kJ/kg)	Entropy (kJ/kg · K)	Quality (%)
1	41.51	0.008	173.84	0.5925	0
2	41.60	0.875	175	0.5934	subcooled
3	70.92	0.875	297.6	0.9658	subcooled
4	103.86	0.875	436.02	1.35	subcooled
5	138.61	0.875	583.55	1.7243	subcooled
6	172.66	0.875	730.76	2.0677	subcooled
7	174.09	7.4418	740.52	2.0732	subcooled
8	212.38	7.4418	910.35	2.4374	subcooled
9	256.48	7.4418	1117.2	2.845	subcooled
9sl	290	7.4418	1290	3.1612	0
9sv	290	7.4418	2766.7	5.7834	100
10	540	7.4418	3503.2	6.889	superheated
11	464.55	4.54	3357.65	6.9189	superheated
12	357.09	2.06	3152.24	6.9684	superheated
13	357.09	2.06	3152.24	6.9684	superheated
14	540	2.06	3556.2	7.5312	superheated
15	414.48	0.875	3297.19	7.5759	superheated
16	302.26	0.3627	3072.64	7.6221	superheated
17	185.95	0.1224	2846.53	7.6808	superheated
18	77.99	0.03461	2641.28	7.7502	superheated
19	41.51	0.008	2448.69	7.8221	94.692
20	46.6	0.03357	195.16	0.6596	subcooled
21	75.92	0.11873	317.94	1.0267	subcooled
22	108.86	0.35182	456.75	1.4061	subcooled
23	179.09	1.9982	759.55	2.129	subcooled
24	217.38	4.4038	932.13	2.4894	subcooled
25	41.51	0.008	2104.49	6.7282	80.364
26sl	400	1.09	800.5	3.3395	0
26	400	1.09	1005.8	3.6445	100
27	369.2	0.239	960.03	3.6552	superheated
28	315.16	0.239	854.05	3.4684	superheated
28sv	300	0.239	825.8	3.4197	100
29	300	0.239	585.97	3.0013	11.567
30	300	0.239	554.6	2.9465	–
31	301	1.09	555.99	2.9512	0
32	345.33	1.09	661.96	3.125	subcooled
33	342.28	–	–	–	–
34	355.33	1	–	–	–
35	440.41	1	–	–	–
36	565	1	–	–	–
37	300	1	–	–	–
38	565	1	–	–	–
39	367.09	1	–	–	–
40	565	1	–	–	–

thinner pipe walls and turbine casings with less expensive materials, leading to a faster dynamic response and lower cost of the SRC.

Aside from the technical and economic benefits, the partial cascade ORC-SRC is more efficient than the conventional SRC. Its efficiency at 290 °C is 45.3%, while the conventional SRC efficiency is less than 42% [22]. The higher efficiency results from a higher average temperature in the heating process. The heating process of the ORC-SRC is composed of three parts: 1) the BDO mixture enthalpy increment from state point 32 to state point 26; 2) the steam enthalpy increment from state point 9sv to state point 10; and 3) the steam enthalpy increment from state point 13 to state point 14. For a conventional SRC, the heating process consists of two parts: 1) the water/steam enthalpy increment from state point 9 to state point 10; and 2) the steam enthalpy increment from state point 13 to state point 14. The average temperatures of the two cycles in the heating process can be expressed by:

$$t_{av,ORC-SRC} = (m_{ORC}\int_{32}^{26} tds + m_{10}\int_{9_{sv}}^{10} tds + m_{13}\int_{13}^{14} tds)/[m_{ORC}(s_{26}-s_{32}) + m_{10}(s_{10}-s_{9_{sv}}) + m_{13}(s_{14}-s_{13})] \quad (57)$$

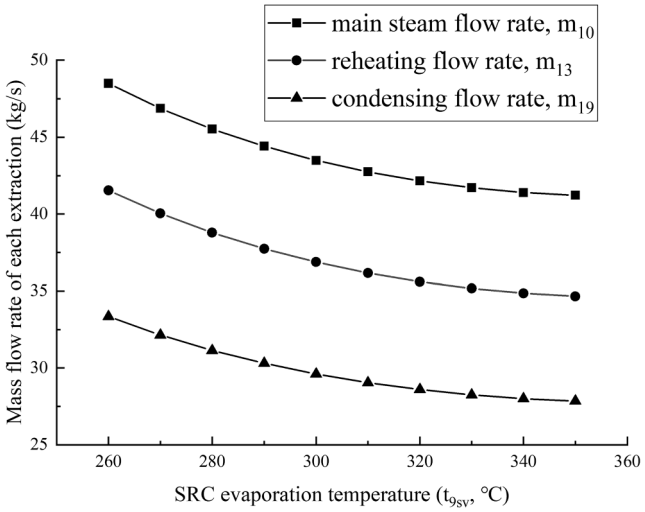

Fig. 6. Variations of the mass flow rates of main steam, reheating and condensing.

$$t_{av,SRC} = (\int_{9}^{10} tds + \int_{13}^{14} tds)/(s_{10} - s_9 + s_{14} - s_{13}) \quad (58)$$

Based on the above expression cancelling out the constant of 273.15, $t_{av,ORC-SRC}$ at t_{9sv} = 290 °C is 402 °C, while $t_{av,SRC}$ is 338 °C for a conventional SRC.

4.1.2. Mass flow rate

All the mass flow rates correlated with the turbines are graphed in Figs. 6 and 7. The flow rates of main steam (m_{10} or m_9), reheating (m_{13}) and condensing (m_{19}) fall down almost linearly. With the increment in t_{9sv}, the power output of the steam turbines per kilogram of steam rises. As the gross electric power of the two turbines is fixed at 50 MWe, m_{10} falls down. The flow rates of the extracted steam are much lower than m_{10}, m_{13} or m_{19}, and range from about 1.5 kg/s to 4.0 kg/s. As $m_{13} = m_{10} - m_{11} - m_{12}$, the decline of m_{10} is greater than the sum of m_{11} and m_{12}, and thereby m_{13} goes down as depicted in Fig. 6. The same is true for m_{19}.

The relative decrements of the extracted steam in the LP turbine are about 10%, similar to those of m_{19}. According to the heat balance in OF, CF-3, CF-4 and CF-5, a decreased m_{19} results in a smaller extraction rate. However, the flow rates of the extracted steam in the HP turbine are flatter, especially for m_{11}. The change in m_{11} is caused by another conflicting factor working in conjunction with m_{19}. In this simulation the extraction pressures are fixed despite a variable steam pressure at the HP turbine inlet. A higher t_{9sv} is accompanied by a higher live steam pressure (p_{10}) while a constant live steam temperature of 540 °C. Given the extraction pressure, t_{11} decreases with a larger steam pressure ratio during expansion in the HP turbine. h_{11} consequently drops, which tends to cause a higher m_{11}.

The mass flow rates of molten salts are shown in Fig. 8. The total mass flow rate of molten salts (m_{ms}) drops moderately, while the three branches show different change trends. Take m_{36} as an instance. Both t_{28} and t_{30} rise as t_{9sv} elevates on account of the heat transfer temperature

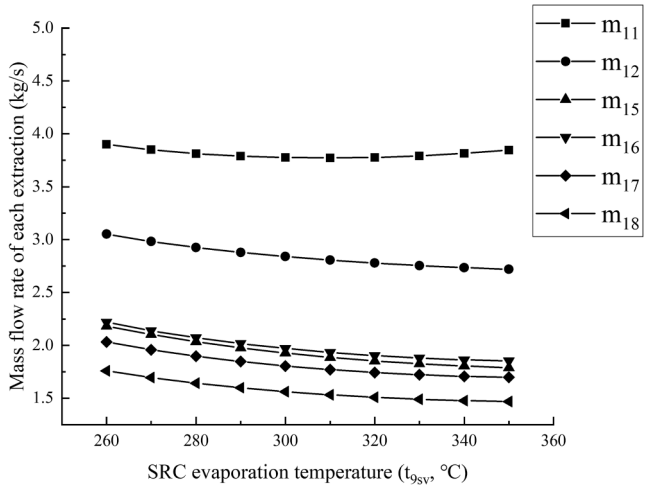

Fig. 7. Variations of the mass flow rate of each extraction.

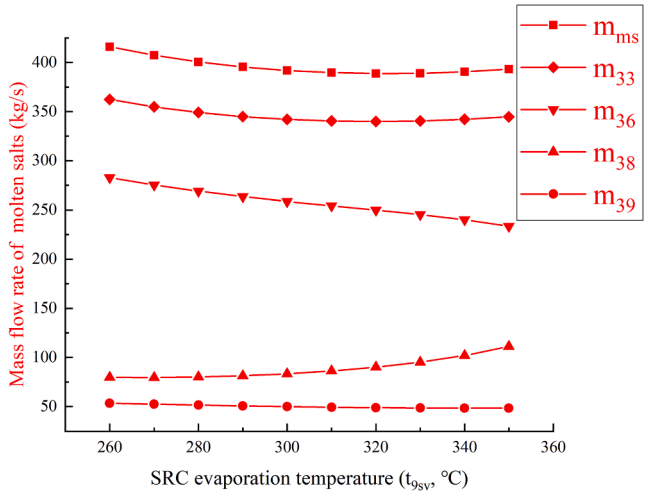

Fig. 8. Variations of the mass flow rate of molten salts.

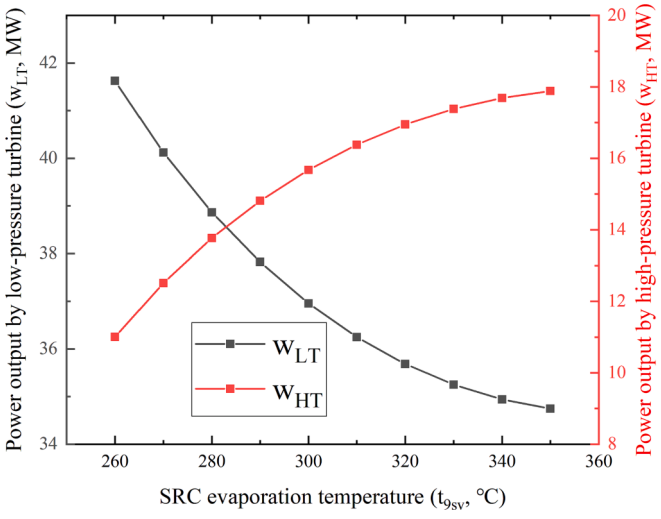

Fig. 9. Variations of power output by the HP and LP turbines.

difference in the steam generator and preheater. Given the ORC evaporation temperature and IHX efficiency, t_{32} and h_{32} increase accordingly. As both m_{ORC} and $(h_{26} - h_{32})$ decline, the heat required by ORC $(m_{ORC}(h_{26} - h_{32}))$ reduces. Simultaneously, the specific heat capacity of molten salts ($c_{p,ms}$) varies marginally in the same temperature interval. It can be deduced that m_{36} goes down based on Eqs. (6) and (7).

4.1.3. Power output

Variations of the power output by the HP and LP turbines are graphed in Fig. 9. w_{HT} increases while w_{LT} decreases as t_{9sv} climbs. w_{LT} is approximately 1.94–3.78 times as much as w_{HT}. The reason for the increment in w_{HT} can be explained by the variations of mass flow rates and enthalpy values. Both m_{10} and m_{13} decrease, and the difference between them is approximately constant as t_{9sv} increases, and the changes in m_{11} and m_{12} are slight. Meanwhile, h_{10}, h_{11}, h_{12} and h_{13} ($h_{12} = h_{13}$) decline as t_{9sv} elevates. But the decrements in h_{11}, h_{12} and h_{13} are more remarkable than those in h_{10}. For instance, the difference between h_{10} and h_{12} is 245.81, 285.38, 320.41 kJ/kg when t_{9sv} is 260, 270, 280 °C, respectively. Although m_{10} decreases, w_{HT} rises with t_{9sv} because of a larger enthalpy drop in the HP turbine. The decrement in the w_{LT} is caused by the decreasing m_{13} and the increasing w_{HT}.

Variations of the net power output of SRC and ORC are exhibited in Fig. 10. w_{SRC} declines marginally while w_{ORC} falls considerably as t_{9sv} elevates. Given the total power output of the steam turbines of 50 MWe, the increment in t_{9sv} leads to more water pump power consumption, so w_{SRC} is slightly reduced. w_{ORC} drops as the ORC condensation temperature rises and the efficiency decreases. w_{SRC} is approximately 3.22–15.64 times as high as w_{ORC}. w_{SRC} is 49.53 MWe and w_{ORC} is 10.30 MWe at the optimal condition of $t_{9sv} = 290$ °C.

4.1.4. t-q Diagram

Fig. 11 (a) and (b) illustrate the *t-q* diagrams at the optimal condition. The dotted lines distinguish different heat exchangers. Given the molten salt inlet temperatures of 565 °C, the minimum heat transfer temperature difference (Δt_{min}) occurs at the molten salt outlets for the four heat exchangers (ORC preheater, ORC evaporator, steam superheater, and steam reheater). The LTT temperature (t_{LTT}) is 345.4 °C according to Eq. (16). When the heat source is the BDO mixture, Δt_{min} takes place at the evaporation point (9_{sl}) for the steam preheater and in the binary phase region for the steam generator. The heat transfer in the ORC preheater, ORC evaporator, steam superheater, steam reheater, steam preheater, steam generator, and IHX is 33.891, 50.223, 32.708, 15.247, 7.674, 65.581, and 25.924 MW, respectively.

Notably, the temperature drop between the two tanks (219.6 °C) is smaller than that in the traditional SPT plants (275 °C). A smaller

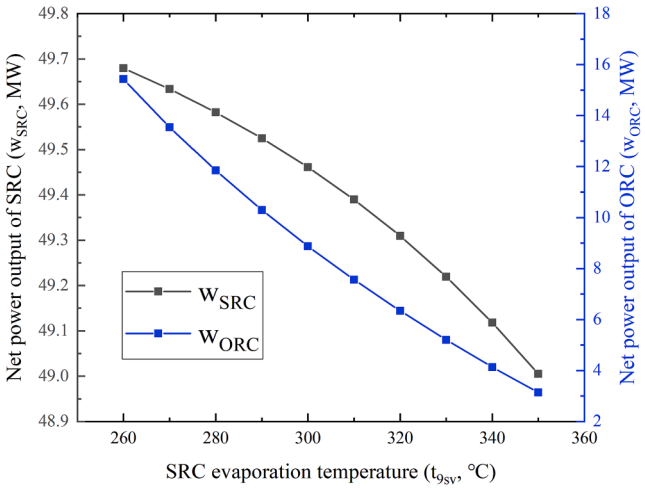

Fig. 10. Variations of the net power output of SRC and ORC.

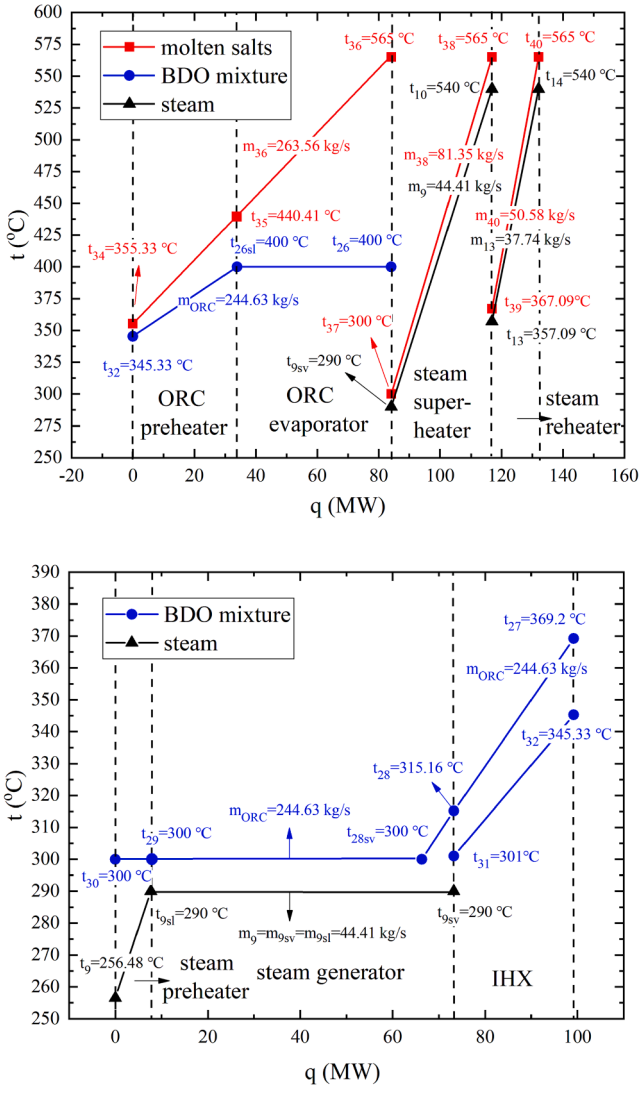

Fig. 11. *t-q* diagrams at the optimal condition.

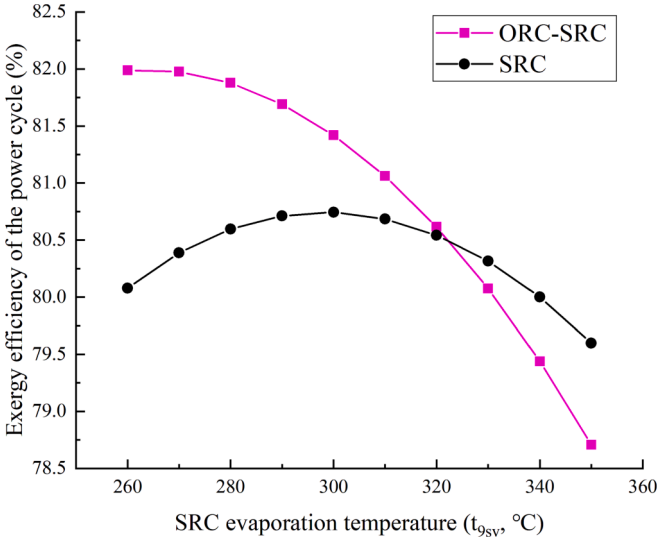

Fig. 12. Variations of the ORC-SRC and SRC exergy efficiencies.

temperature drop indicates less heat release per mass of molten salts. More salts will be needed at a given storage capacity, which could be a disadvantage for the proposed novel structure. Section 4.2 will consider this impact and evaluate the thermo-economic performance.

4.1.5. Exergy analysis

Variations of the ORC-SRC exergy efficiency ($\eta_{ex,ORC-SRC}$) and the SRC exergy efficiency ($\eta_{ex,SRC}$) are illustrated in Fig. 12. $w_{ORC-SRC}$ is 65.111 , 59.823 , 55.650 and 52.139 MW when t_{9sv} is 260, 290, 320 and 350 °C, while the exergy consumed by the ORC-SRC ($Ex_{ORC-SRC}$) is respectively 79.416, 73.231, 69.032 and 66.244 MW. The relative decrease of $w_{ORC-SRC}$ is slightly larger than that of $Ex_{ORC-SRC}$, and it can be deduced that $\eta_{ex,ORC-SRC}$ goes down according to Eq. (40). The change in $\eta_{ex,SRC}$ can similarly be explained by Eq. (39). The maximum $\eta_{ex,ORC-SRC}$ is 81.99% when t_{9sv} = 260 °C, while the maximum $\eta_{ex,SRC}$ is 80.74% when t_{9sv} = 300 °C. $\eta_{ex,ORC-SRC}$ is higher than $\eta_{ex,SRC}$ when t_{9sv} rises from 260 °C to 322 °C, which indicates that the cascade cycle has a higher degree of thermodynamic perfection than the single SRC in the low t_{9sv} range.

The exergy losses in ORC-SRC at the optimum condition are shown in Fig. 13. The total exergy destructions are 14.27 MW. The largest exergy destruction takes place in the condenser, followed by the ORC evaporator and LP turbine. They account for two thirds of the total losses. Though the LP turbine is more efficient than the HP turbine, the irreversible loss of the former is significantly higher due to a larger enthalpy drop (i.e., exergy drop) during expansion. The irreversible losses in P1 and P2 account for 0.07% and 0.51%, respectively, which are much less than those of P3. The reason is that the mass flow rate through P3 (m_{ORC} = 244.63 kg/s) is noticeably larger than that of P1 (m_1 = 35.77 kg/s) and P2 (m_6 = 44.41 kg/s).

4.2. Thermo-economics analysis

Given the solar field and SRC, the proposed system has additional investments in the ORC and molten salts. The following sections will estimate the cost of heat exchangers, other equipment and material cost, annual electricity yield, and equivalent payback period (*EPP*).

4.2.1. Cost of heat exchangers

The cost of large heat exchangers is mainly determined by the heat transfer area and hence the total amount of materials in use [56]. HTRI software is the industry's most advanced thermal process design and simulation software [65], and it is used to estimate the area of the IHX, ORC preheater, and evaporator. The physical parameters of the BDO mixture can be derived from Aspen Plus [66] by importing a mass fraction of 26.5% biphenyl and 73.5% diphenyl oxide. Then the parameters like density, heat capacity, thermal conductivity and viscosity can be imported from Aspen Plus into HTRI. A BFM-type fixed tubesheet heat exchanger with double tubepasses and a single shell side is adopted on account of its wide application and simple structure. The fluid with higher pressure is located in the tube side to reduce the fabricating cost. Rod baffle is utilized to reduce the vibration and the flow resistance of the shell side fluid. A tube outer diameter of 19 mm and a tube pitch of 25 mm are employed, which are common in industrial production.

It is difficult to accurately calculate the BDO mixture temperature at superheated (27 and 28) or subcooled (31 and 32) states according to the saturation pressure and enthalpy. Nevertheless, given the heat capacity and heat exchanger structure, the heat transfer coefficient is affected comprehensively by the inlet and outlet temperatures, pressures, and flow rates, as well as the physical properties of fluids and the likelihood of phase change. It can be predicted that a deviation of several Celsius degrees of the inlet or outlet temperature has little effect on the design area of a heat exchanger. Take point 27 as an example, according to the conservation of energy, $q = m_{ORC}(h_{27}-h_{28sv}) = m_{ORC} \bullet \overline{c_p} \bullet (T_{27} - T_{28sv})$. Where $\overline{c_p}$ is the average specific heat capacity

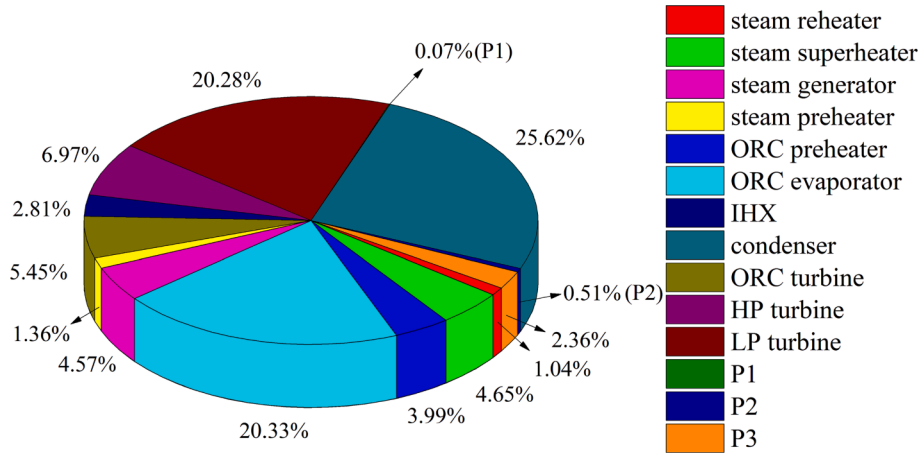

Fig. 13. Exergy losses in the ORC-SRC.

Table 7
Design parameters of the IHX, ORC preheater and ORC evaporator for System I.

Process data	IHX	ORC preheater	ORC evaporator
Shell side heat transfer coefficient, kW/m^2·K	1.314	0.866	2.378
Shell ID, mm	2000	1900	1100
Shell side velocity, m/s	34.79	0.19	0.59
Tube side heat transfer coefficient, kW/m^2·K	1.639	1.697	6.493
Tube length, m	13	18	9
Tube side velocity, m/s	0.88	0.92	23.28
Tube count	4062	4122	1303
Overall heat transfer coefficient, kW/m^2·K	0.505	0.442	1.014
Heat duty, MW	31.008	35.307	52.033
Inlet/Outlet height under nozzles, mm	0	0	0
Baffle central spacing, mm	500	1000	1000
Effective mean temperature difference, °C	21.8	20.6	88.0
Area, m^2	3106.60	4377.62	660.48
Over design, %	10.15	12.96	13.19

and $\overline{c_p} = (c_{p27} + c_{p28sv})/2$. c_{p27} can be deduced approximately by linear interpolation based on h_{27} and the saturated vapor parameters, as there is little difference between the specific heat capacity of saturated vapor and superheated vapor when the enthalpy is the same. It can be obtained $c_{p27} = 2.04$ kJ/(kg • K) and $t_{27} = 377.94$ °C. Analogously, $c_{p28} = 1.89$ kJ/(kg • K) and $t_{28} = 315.16$ °C.

The fouling resistances of molten salts for heat transfer purposes and the organic heat carriers for industrial use are 8.8 and 17.6 × 10^{-5} m^2 • K/W respectively according to GB/T 151–2014 [67]. They are taken as the fouling resistances of the molten salts and the BDO mixture in this work. The ratio of the tube length and the shell inner diameter is limited to 4–10, and the over-design area above 10% is ensured in the design process. The output data is listed in Table 7. The schemes of the three heat exchangers are displayed in Fig. 14. The investments in IHX, ORC preheater, ORC evaporator, ORC turbine, ORC generator, and P3 are respectively 118.631, 159.053, 38.305, 233.312, 40.147, and 21.379 × 10^4 $.

4.2.2. Equivalent payback period

The *EPP* represents the economic advantage of the ORC-SRC over a conventional SRC. In the comparison, the SRC in both cycles has a power output of 50 MWe. $\eta_{SRC,ref}$ is assumed to be 42.3%, and this value is consistent with η_{SRC} in Fig. 5 at $t_{9sv} = 330$ °C ($p_{10} = 12.86$ MPa). The operation pressure is close to those of recent SPT plants in Table 1, such as Crescent Dunes Solar Energy Project, Shouhang Dunhuang Phase II – 100 MWe Tower, and the reference project. $\eta_{SRC,ref}$ is also close to the design value of 41.98% in the literature [22].

For the referenced Delingha 50 MWe Tower project, the required molten salts mass, annual electricity generation, levelized cost of electricity, and storage capacity are 10,093 tonnes, 146 GWh, 0.09 $/kWh, and 7 h respectively based on the available data [11,51]. The power generated by the ORC turbine (w_{OT} • ε_g) is 10637.62 kW according to Eq. (23) and M_{BDO} is 57443–59252 kg according to Section 3.2.4. For sufficient charge mass and reliable results, M_{BDO} is taken as 60 tonnes and C_{BDO} is 13.2 × 10^4 $. Notably, the BDO mixture has low toxicity and causes little harm to the human body and the environment [68]. It is a widely used industrial heat transfer fluid. As it runs in a closed circulation space in the proposed system, the risk of leakage is low, and the mass is negligible compared to that used in commercial large PTC systems. Extra 2509.65 tonnes of molten salts are required by System I and the related extra cost of molten salts ($C_{ms,extra}$) is 125.48 × 10^4 $. System I is expected to generate an excess power output of 1035.46 × 10^4 kWh (i.e., 190.525 × 10^4 $ revenue) per year at the additional cost of 665.22 × 10^4 $. The *EPP* regarding the implementation of the ORC on the 50 MWe reference project is therefore within 3.93 years.

4.3. Comparison between systems I and II

Variations of ORC-SRC efficiencies of the two systems are illustrated in Fig. 15. The variation of $\eta_{ORC-SRC}$ has been explained in Section 4.1.1. Given t_{9sv}, $\eta_{ORC-SRC}$ of System I is higher than that of System II. Their maximum values of 45.30% and 44.99% are achieved at t_{9sv} of 290 °C and 270 °C, respectively.

Variations of the LTT temperatures are exhibited in Fig. 16. For System I, t_{LTT} is determined comprehensively by t_{37}, t_{34}, t_{39} and the correlated m_{37}, m_{34}, m_{39}. t_{37} and t_{34} rise while t_{39} drops as t_{9sv} increases based on Eq. (8). As shown in Fig. 8, m_{33} ($m_{33} = m_{37} + m_{34}$) is much larger than m_{39}. It can be deduced from Section 3.1.2 that t_{LTT} goes up. t_{LTT} for System II can be analyzed in a similar way. The HTT temperatures for both systems are fixed at 565 °C. For System II, a larger temperature difference between the molten salt tanks is obtained, which indicates that the storage capacity is higher at a given amount of molten salts. However, the superiority in the temperature drop is not evident at their optimum steam evaporation temperatures (219.6 °C by System I vs. 231.24 °C by System II).

The additional heat exchange areas for System II are summarized in Table 8. The investments in IHX, ORC preheater, ORC evaporator, ORC turbine, ORC generator, and P3 are respectively 136.658, 192.504, 36.904, 232.469, 49.804, and 22.040 × 10^4 $. The power generated by the ORC turbine (w_{OT} • ε_g) is 13346.89 kW. M_{BDO} is taken as 75 tonnes

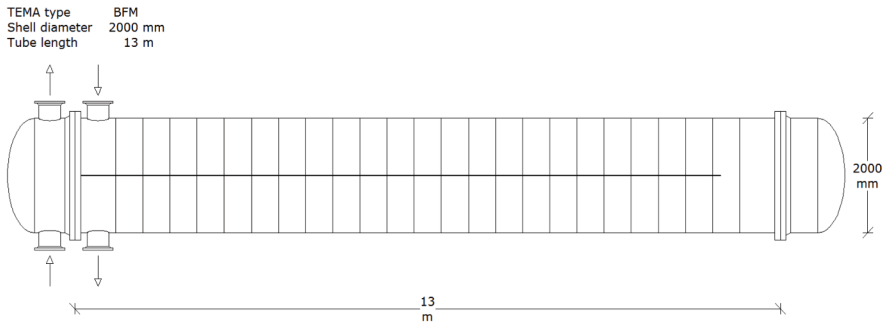

(a) Scheme of the IHX.

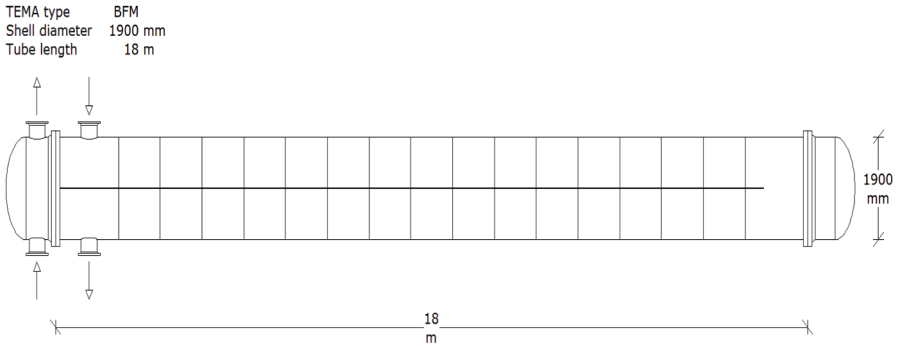

(b) Scheme of the ORC preheater.

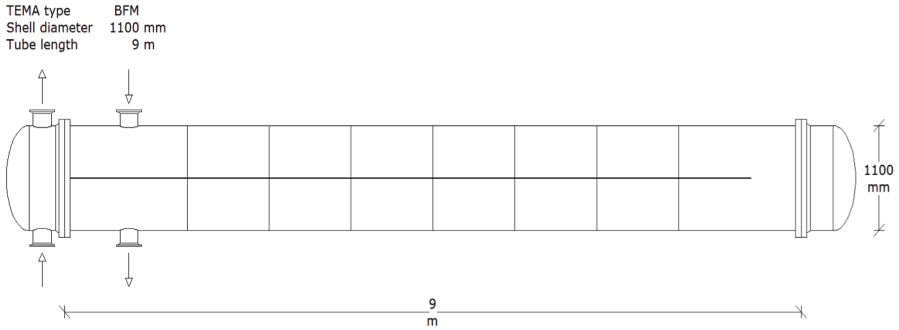

(c) Scheme of the ORC evaporator.

Fig. 14. Schemes of the shell and tube heat exchangers.

and C_{BDO} is 16.5×10^4 \$. Extra 1880.26 tonnes of molten salts are needed and $C_{ms,extra}$ is 94.012×10^4 \$. System II is expected to generate an excess power output of 928.46×10^4 kWh (i.e., 170.837×10^4 \$ revenue) per year at the additional cost of 780.89×10^4 \$. *EPP* is 4.57 years for System II.

5. Future work

In this simulation, the thermodynamic optimization focuses on the steam generation temperature. The steam reheat and extraction pressures are fixed for a preliminary analysis of the proposed system. However, the steam reheat pressure is an influential factor in the SPT efficiency [52], and so are the extraction pressures. As the steam generation temperature and pressure change, the optimum reheat and extraction pressures may vary. The proposed system is expected to have even higher efficiency in optimizing these parameters.

The heat transfer optimization will also enlarge the storage capacity. The novel system has a smaller temperature drop of molten salts than conventional SPT systems. A more efficient heat exchanger network can be designed. For instance, two-stage steam reheaters and superheaters can be used. They may reduce the heat transfer irreversibility between molten salts and power cycle fluids and provide a lower t_{LTT}.

Working fluids play an important role in ORC performance. The BDO mixture has a maximum operating temperature of about 400 °C. Fluids of higher evaporation temperature, such as liquid metals, may further increase $\eta_{ORC-SRC}$ and can be explored.

6. Conclusion

A novel partial cascade ORC-SRC integrated with dual-tank molten salt storage is proposed in this paper. It is equipped with a top BDO mixture-based ORC to increase the heat-to-power conversion efficiency while avoiding the challenges associated with supercritical cycles. The main conclusions are summarized as follows:

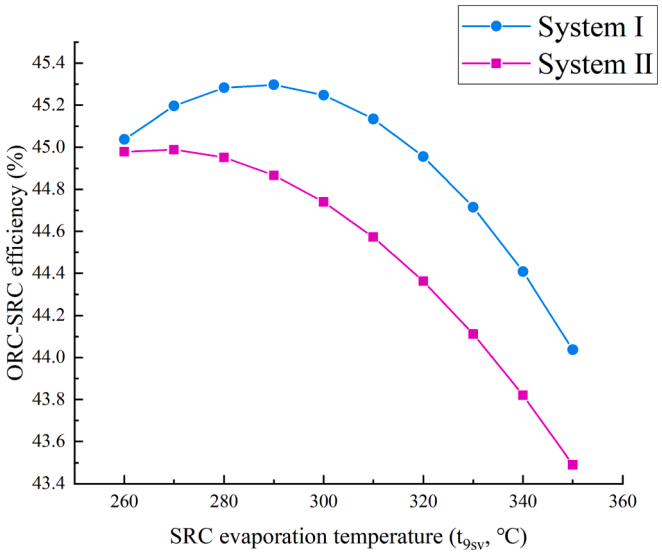

Fig. 15. Variations of ORC-SRC efficiencies of the two systems.

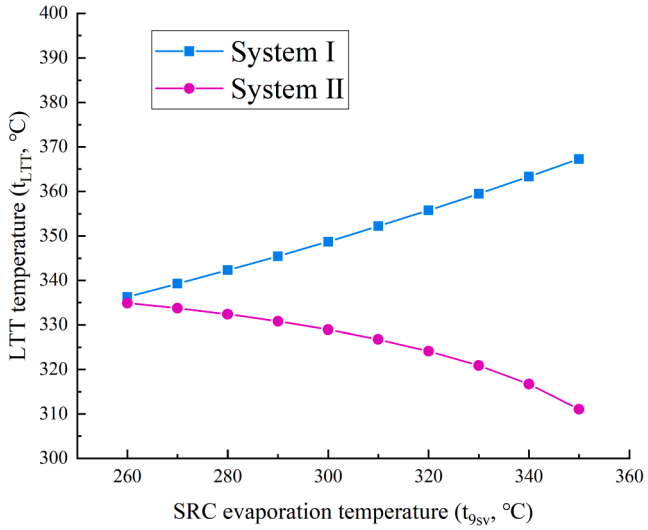

Fig. 16. Variations of LTT temperatures of the two systems.

Table 8
Design parameters of the IHX, ORC preheater, and ORC evaporator for System II.

Process data	IHX	ORC preheater	ORC evaporator
Shell side heat transfer coefficient, kW/m^2·K	1.035	0.788	2.390
Shell ID, mm	2200	2000	1100
Shell side velocity, m/s	40.57	0.17	0.59
Tube side heat transfer coefficient, kW/m^2·K	1.337	1.525	6.446
Tube length, m	12.5	20	8.5
Tube side velocity, m/s	0.67	0.80	23.41
Tube count	4999	4582	1303
Overall heat transfer coefficient, kW/m^2·K	0.423	0.406	1.014
Heat duty, MW	35.139	41.540	50.814
Inlet/Outlet height under nozzles, mm	0	0	0
Baffle central spacing, mm	900	1000	1000
Effective mean temperature difference, °C	25.8	21.4	90.8
Area, m^2	3669.08	5409.37	621.60
Over design, %	13.89	13.33	12.68

The average temperature of the power cycle in the heating process increases from 338 °C to 402 °C as the ORC-SRC is in place. The maximum $\eta_{ORC-SRC}$ of 45.3% is achievable at t_{9sv} of 290 °C. It is appreciably higher than the efficiencies of 41.2–41.98% obtained by the conventional SPT plants. Meanwhile, the HP steam turbine inlet pressure is lower than that of common CSP plants (7.44 MPa vs. 10–14 MPa), which can reduce turbine loss and cost. w_{SRC} is 49.53 MWe and w_{ORC} is 10.3 MWe at this optimal condition. Nevertheless, the temperature drop between the two tanks is smaller than the traditional value (219.6 °C vs. 275 °C), indicating that a higher heat-to-power generation efficiency is at the sacrifice of the storage capacity per mass of molten salts.

The partial cascade ORC-SRC has a higher degree of thermodynamic perfection at a lower t_{9sv}. The maximum $\eta_{ex,ORC-SRC}$ is 81.99% when t_{9sv} is 260 °C. The largest irreversible loss occurs in the condenser, followed by the ORC evaporator and LP turbine. The three components account for two thirds of the total exergy destruction.

Taking the power capacity and storage capacity of an operating 50 MWe SPT project in China as the reference, the novel system can generate excess electricity of 1035.46 × 10^4 kWh per year at an additional cost of 665.22 × 10^4 $. The equivalent payback time regarding the top ORC is 3.93 years.

CRediT authorship contribution statement

Pengcheng Li: Data curation, Investigation, Methodology, Formal analysis, Writing – original draft. **Tongle Qian:** Resources, Software. **Jing Li:** Conceptualization, Formal analysis, Funding acquisition, Investigation, Methodology, Writing – review & editing. **Haiwei Lin:** Formal analysis, Writing – review & editing. **Yandong Wang:** Resources, Software. **Gang Pei:** Writing – review & editing. **Desuan Jie:** Writing – review & editing. **Dongming Liu:** Writing – review & editing.

Declaration of Competing Interest

The authors declare that they have no known competing financial interests or personal relationships that could have appeared to influence the work reported in this paper.

Data availability

No data was used for the research described in the article.

Acknowledgment

This study was sponsored by National Natural Science Foundation of China (52206008), Fundamental Research Funds for the Central Universities of China (JZ2022HGTB0266), DONGFANG ELECTRIC Dongfang Boiler Group CO., LTD., Science and Technology Major Project of Anhui Province (202003a05020025). The study was improved through an application for Engineering and Physical Sciences Research Council grant (EP/Y001885/1).

References

[1] Palacios A, Barreneche C, Navarro ME, Ding Y. Thermal energy storage technologies for concentrated solar power-A review from a materials perspective. Renew Energy 2020;156:1244–65. https://doi.org/10.1016/j.renene.2019.10.127.
[2] Concentrating Solar Power https://atb.nrel.gov/electricity/2022/concentrating_solar_power. [accessed 7 July 2022].
[3] He YL, Qiu Y, Wang K, Yuan F, Wang WQ, Li MJ, et al. Perspective of concentrating solar power. Energy 2020;198:117373. https://doi.org/10.1016/j.energy.2020.117373.
[4] IRENA. Data & statistics. International Renewable Energy Agency (IRENA).
[5] NREL. System Advisor Model version (SAM) 2020.1.17. National Renewable Energy Laboratory; https://sam.nrel.gov/download.html. [Accessed 16 Aug 2022].
[6] Islam MT, Huda N, Abdullah AB, Saidur R. A comprehensive review of state-of-the-art concentrating solar power (CSP) technologies: Current status and research

trends. Renew Sust Energy Rev 2018;91:987–1018. https://doi.org/10.1016/j.rser.2018.04.097.
[7] Conroy T, Collins MN, Grimes R. A review of steady-state thermal and mechanical modelling on tubular solar receivers. Renew Sust Energy Rev 2020;119:109591. https://doi.org/10.1016/j.rser.2019.109591.
[8] Behar O, Grange B, Flamant G. Design and performance of a modular combined cycle solar power plant using the fluidized particle solar receiver technology. Energy Convers Manage 2020;220:113108. https://doi.org/10.1016/j.enconman.2020.113108.
[9] Patil VR, Kiener F, Grylka A, Steinfeld A. Experimental testing of a solar air cavity-receiver with reticulated porous ceramic absorbers for thermal processing at above 1000 ℃. Sol Energy 2021;214:72–85. https://doi.org/10.1016/j.solener.2020.11.045.
[10] Merchán RP, Santos MJ, Medina A, Hernández AC. High temperature central tower plants for concentrated solar power: 2021 overview. Renew Sust Energy Rev 2022;155:111828. https://doi.org/10.1016/j.rser.2021.111828.
[11] NREL. Concentrating solar power projects. National Renewable Energy Laboratory (NREL); Accessed time: Feb. 18, 2020, www.nrel.gov/csp/solarpaces/index.cfm.
[12] https://new.qq.com/omn/20220701/20220701A077UV00.html. [accessed 9 July 2022].
[13] Gauché P, Rudman J, Mabaso M, Landman WA, Backström TW, Brent AC. System value and progress of CSP. Sol Energy 2017;152:106–39. https://doi.org/10.1016/j.solener.2017.03.072.
[14] Calderón A, Palacios A, Barreneche C, Segarra M, Prieto C, Rodriguez-Sanchez A, et al. High temperature systems using solid particles as TES and HTF material: a review. Appl Energy 2018;213:100–11. https://www.sciencedirect.com/science/article/pii/S0306261917318329.
[15] Baumgartner R. Advanced Coal Technology to Power the World. Siemens Power Generation, Germany: World Bank Energy Week; 2006.
[16] Wibberley L, Cottrell A, Palfreyman D, Scaife P, Brown P. TechnoEconomic Assessment of Power Generation Options for Australia. Technology Assessment Report 2006;52.
[17] Pacheco JE, Wolf T, Muley N. Incorporating Supercritical Steam. Turbines into Advanced Molten-Salt Power Tower Plants: Feasibility and Performance. https://doi.org/10.2172/1088078.
[18] Peterseima JH, Veeraragavan A. Solar towers with supercritical steam parameters - is the efficiency gain worth the effort ? Energy Procedia 2015;69:1123–32. https://doi.org/10.1016/j.egypro.2015.03.181.
[19] Piwowarski M. Optimization of steam cycles with respect to supercritical parameters. Pol Marit Res 2009;16:45–51. https://doi.org/10.2478/v10012-008-0043-3.
[20] White MT, Bianchi G, Chai L, Tassou SA, Sayma AI. Review of supercritical CO_2 technologies and systems for power generation. Appl Therm Eng 2021;185:116447. https://doi.org/10.1016/j.applthermaleng.2020.116447.
[21] IBRAHIM MOHAMED OR. Study of Energy Efficient Supercritical Coal-Fired Power Plant Dynamic Responses and Control Strategies. PhD Thesis, University of Birmingham. https://etheses.bham.ac.uk/id/eprint/3662/.
[22] Li X, Jin J, Yang D, Xu N, Wang Y, Mi X. Comparison of tower and trough solar thermal power plant efficiencies in different regions of China based on SAM simulation. AIP Conf Proc 2019;2126:030033. https://doi.org/10.1063/1.5117545.
[23] González-Roubaud E, Pérez-Osorio D, Prieto C. Review of commercial thermal energy storage in concentrated solar power plants: Steam vs. molten salts. Renew Sust Energ Rev 2017;80:133–48. https://doi.org/10.1016/j.rser.2017.05.084.
[24] Dumont O, Frate GF, Pillai A, Lecompte S, paepe MD, Lemort V. Carnot battery technology: A state-of-the-art review. J Energy Storage 2020;32:101756. https://doi.org/10.1016/j.est.2020.101756.
[25] Vecchi A, Knobloch K, Liang T, Kildahl H, Sciacovelli A, Engelbrecht K, et al. Carnot Battery development: A review on system performance, applications and commercial state-of-the-art. J Energy Storage 2022;55:105782. https://doi.org/10.1016/j.est.2022.105782.
[26] Angamos power station. https://www.gem.wiki/Angamos_power_station.
[27] Wieland C, Dawo F, Schifflechner C, Astolf M. Market report on Organic Rankine Cycle power systems: recent developments and outlook. 6th International Seminar on ORC Power Systems, October 11-13, 2021, Munich, Germany.
[28] Boukelia T.E, Arslan.O, Bouraoui.A. Thermodynamic performance assessment of a new solar tower-geothermal combined power plant compared to the conventional solar tower power plant. Energy 2021;232:121109. https://doi.org/10.1016/j.energy.2021.121109.
[29] Liang Y, Chen J, Luo X, Chen J, Yang Z, Chen Y. Simultaneous optimization of combined supercritical CO2 Brayton cycle and organic Rankine cycle integrated with concentrated solar power system. J Clean Prod 2020;266:121927.
[30] Han X, Zhao G, Xu C, Ju X, Du X, Yang Y. Parametric analysis of a hybrid solar concentrating photovoltaic/concentrating solar power (CPV/CSP) system. Appl Energy 2017;189:520–33. https://doi.org/10.1016/j.apenergy.2016.12.049.
[31] Vescovo R. High temperature organic rankine cycle (HT-ORC) for cogeneration of steam and power. AIP Conference Proceedings 2019;2191:020153. https://doi.org/10.1063/1.5138886.
[32] Vescovo R, Spagnoli E. High Temperature ORC Systems. Energy Procedia 2017;129:82–9. https://doi.org/10.1016/j.egypro.2017.09.160.
[33] Sampedro EO, Védie L. Wet to dry cycles for high temperature waste heat valorization using a diphenyl biphenyl oxide mixture. In: 6th International Seminar on ORC Power Systems, October 11-13, 2021, Munich, Germany. https://mediatum.ub.tum.de/doc/1633030/1633030.pdf.
[34] Bombarda P, Invernizzi C. Binary liquid metal–organic Rankine cycle for small power distributed high efficiency systems. Proc IMechE Part A: J Power and Energy 2014;229(2):192–209. https://doi.org/10.1177/0957650914562094.
[35] SolarPACES. CSP projects around the world. 2022 http://www.solarpaces.org/csp-technology/csp-projects-around-the-world. [Accessed 17 Aug 2022].
[36] Niggemann RE. Quarterly Progress Report No. 12 - Organic Rankine Cycle Technology Program. Report, Sundstrand Corporation. Report No. SAN-651-96 Prepared under contract AT (04-3)-651 for the San Francisco Operations Office U. S. Atomic Energy Commission, 15 April 1969. https://doi.org/10.2172/4774929.
[37] Anderson WG. Intermediate temperature fluids for heat pipes and loop heat pipes. In: 15th International heat pipe conference, Clemson, USA, 25-30 April 2010.
[38] Bronicki LY. The Ormat Rankine power unit. In:7th Intersociety energy conversion engineering conference, San Diego, USA, 1972, pp. 327-34.
[39] Turboden S.p.A., BRUNL, Cogenerative organic Rankine cycle system. International Publication Number: WO2017/199170A1, 23 Nov 2017.
[40] Angelino G, Invernizzi C. Binary conversion cycles for concentrating solar power technology. Sol Energy 2008;82:637–47. https://doi.org/10.1016/j.solener.2008.01.003.
[41] Eastman Corp; https://www.eastman.com/Literature_Center/T/TF9141.pdf [accessed 3 May 2022].
[42] Wang WQ, Qiu Y, Li MJ, He YL, Cheng ZD. Coupled optical and thermal performance of a fin-like molten salt receiver for the next-generation solar power tower. Appl Energy 2020;272:115079. https://doi.org/10.1016/j.apenergy.2020.115079.
[43] Mohammadi K, McGowan JG. Thermodynamic analysis of hybrid cycles based on a regenerative steam Rankine cycle for cogeneration and trigeneration. Energy Convers Manage 2018;158:460–75. https://doi.org/10.1016/j.enconman.2017.12.080.
[44] Baumann K. Some recent developments in large steam turbine practice. Engineer 1921;59(302):565–623. https://doi.org/10.1049/JIEE-1.1921.0040.
[45] Gao G, Li J, Li P, Cao J, Pei G, Dabwana YN, et al. Design of steam condensation temperature for an innovative solar thermal power generation system using cascade Rankine cycle and two-stage accumulators. Energy Convers Manage 2019;184:389–401. https://doi.org/10.1016/j.enconman.2019.01.067.
[46] THERMINOL® Heat Transfer Fluids by Eastman. ≤https://www.therminol.com/> [accessed 18 Jan 2023].
[47] Li P, Li J. High temperature direct vapor generation organic Rankine cycle in the concerntrated solar power application. 6th International Seminar on ORC Power Systems, October 11-13, 2021, Munich, Germany.
[48] Li J, Alvi JZ, Pei G, Su Y, Li P, Gao G, et al. Modelling of organic Rankine cycle efficiency with respect to the equivalent hot side temperature. Energy 2016;115:668–83. https://doi.org/10.1016/j.energy.2016.09.049.
[49] Gao G, Li J, Li P, Yang H, Pei G, Ji J. Design and analysis of an innovative concentrated solar power system using cascade organic Rankine cycle and two-tank water/steam storage. Energy Convers Manage 2021;237:114108. https://doi.org/10.1016/j.enconman.2021.114108.
[50] Xu C, Wang Z, Li X, Sun F. Energy and exergy analysis of solar power tower plants. Appl Therm Eng 2011;31(17–18):3904–13. https://doi.org/10.1016/j.applthermaleng.2011.07.038.
[51] Blue Book of China's Concentrating Solar Power Industry 2021.
[52] Rodríguez-Sanchez MR, Sanchez-Gonzalez A, Gonzalez-Gomez PA, Marugan-Cruz C, Santana D. Thermodynamic and economic assessment of a new generation of subcritical and supercritical solar power towers. Energy 2017;118:534–44. https://doi.org/10.1016/j.energy.2016.10.079.
[53] Zhang C, Liu C, Wang S, Xu X, Li Q. Thermo-economic comparison of subcritical organic Rankine cycle based on different heat exchanger configurations. Energy 2017;123:728–41. https://doi.org/10.1016/j.energy.2017.01.132.
[54] Li J, Hu S, Yang F, Duan Y, Yang Z. Thermo-economic performance evaluation of emerging liquid-separated condensation method in single-pressure and dual-pressure evaporation organic Rankine cycle systems. Appl Energy 2019;256:113974. https://doi.org/10.1016/j.apenergy.2019.113974.
[55] Turton R, Bailie RC, Whiting WB, Shaeiwit JA, Bhattacharyya D. Analysis, synthesis, and design of chemical processes. Pearson Education Inc; 2009.
[56] Cataldo F, Mastrullo R, Mauro AW, Vanoli GP. Fluid selection of organic Rankine cycle for low-temperature waste heat recovery based on thermal optimization. Energy 2014;72:159–67. https://doi.org/10.1016/j.energy.2014.05.019.
[57] REKKAS-VENTIRIS, GEORGIOS, Archimede Concentrated Solar Power Plant Dynamic Simulation: Control systems, Heat Transfer Fluids and Thermal Energy Storage, 2018.
[58] Bai L. Life cycle assessment of electricity generation from low temperature waste heat: the influence of working fluid. NTNU-Norwegian University of Science & Technology; 2012.
[59] Ding Y, Liu C, Zhang C, Xu X, Li Q, Mao L. Exergoenvironmental model of Organic Rankine Cycle system including the manufacture and leakage of working fluid. Energy 2018;145:52–64. https://doi.org/10.1016/j.energy.2017.12.123.
[60] Li J, Gao G, Kutlu C, Liu K, Pei G, Su Y, et al. A novel approach to thermal storage of direct steam generation solar power systems through two-step heat discharge. Appl Energy 2019;236:81–100. https://doi.org/10.1016/j.apenergy.2018.11.084.
[61] Padilla RV. Simplified Methodology for Designing Parabolic Trough Solar Power Plants. University of South Florida. Graduate School Theses and Dissertations 2011.
[62] Montes MJ, Abánades A, Martínez-Val JM, Valdés M. Solar multiple optimization for a solar-only thermal power plant, using oil as heat transfer fluid in the parabolic trough collectors. Sol Energy 2009;83(12):2165–76. https://doi.org/10.1016/j.solener.2009.08.010.

[63] Chacartegui R, Vigna L, Becerra JA, Verda V. Analysis of two heat storage integrations for an Organic Rankine Cycle Parabolic trough solar power plant. Energy Convers Manage 2016;125:353–67. https://doi.org/10.1016/j.enconman.2016.03.067.
[64] Delgado-Torres AM, García-Rodríguez L. Analysis and optimization of the low-temperature solar organic Rankine cycle (ORC). Energy Convers Manage 2010;51(12):2846–56. https://doi.org/10.1016/j.enconman.2010.06.022.
[65] HTRI Software; 2020. <https://www.htri.net/> [accessed 3 May 2022].
[66] https://www.aspentech.com/en/products/engineering/aspen-plus.[Accessed 6 September 2022].
[67] Fouling resistance of industrial fluids. National Standard of the People's Republic of China. GB/T 151-2014. pp. 212-13.
[68] SAFETY DATA SHEET Therminol VP1 Heat Transfer Fluid; https://americasinternational.com/wp-content/uploads/2020/03/THERMINOL-VP1-SDS-EASTMAN.pdf [accessed 18 Jan 2023].